2020

Electrical characterization of 316L metal powder used in additive manufacturing

Joseph Talbot Filbert
Iowa State University

Electrical characterization of 316L metal powder used in additive manufacturing

by

Joseph Talbot Filbert

A thesis submitted to the graduate faculty

in partial fulfillment of the requirements for the degree of

MASTER OF SCIENCE

Major: Electrical Engineering (Electromagnetics, Microwave, and Nondestructive Evaluation)

Program of Study Committee:
Nicola Bowler, Major Professor
Jiming Song
David Jiles

The student author, whose presentation of the scholarship herein was approved by the program of study committee, is solely responsible for the content of this thesis. The Graduate College will ensure this thesis is globally accessible and will not permit alterations after a degree is conferred.

Iowa State University

Ames, Iowa

2020

DEDICATION

I would like to dedicate this thesis to my mother Kimberly, without her continual, unwavering support I would never have made it this far.

TABLE OF CONTENTS

Page

LIST OF TABLES

LIST OF FIGURES

ACKNOWLEDGMENTS

I would like to express my sincere gratitude to those who have helped me with conducting this research and writing this thesis. First, I am particularly grateful to Dr. Nicola Bowler for her guidance and support in all aspects of this research as well as her invaluable mentorship which has helped me to navigate my academic career and to plot the course of my professional career. Additionally, the continued interest and support of Dr. Andrew Gavens of KAPL was instrumental to the completion of this research and my personal academic success. I am grateful to the research teams at the Naval Nuclear Laboratory who were able to provide Auger electron spectroscopy, optical microscopy, and secondary electron microscopy data, Michael Burrell and Jessica Pyle. I would also like to thank Dr. Steve Martin for the use of the Novocontrol dielectric spectrometer with a special thank you to Steven Kmiec for training me to use the instrument and software. Also, I would like to thank the other members of the electromagnetic materials design and characterization group Aishwarya Sriraman, Trishelle Copeland-Johnson and Callie Gifford for their support and interest in the development and progress of this research. I would also like to thank the support of my partner Theressa, who over the last seven years has put up with my long nights of studying and pacing in front of my whiteboards, as well as the munchkins Jessika and William. Lastly, I would like to thank my brother Jeremy for his support and patience while I poorly attempt to explain what I'm working on during our phone calls.

ABSTRACT

This research explores the feasibility of using the electrical properties of a metal powder to characterize the overall quality of the powder for use in powder bed fusion additive manufacturing. Feed powder which is recycled over multiple build cycles will no longer build quality parts; manufacturers and operators are interested in the ability to measure the powder degradation over time, to determine when the feed powder needs to be replaced or refreshed. The effects of reuse have been monitored using both chemical and mechanical characterization tests. The characterization tests investigate the particle size distribution (PSD), density, morphology, and surface chemistry of the feed powder. Additionally, strength and ductility of the built parts have also been assessed using mechanical testing, allowing correlation of the feed powder properties with the built part quality. Mechanical and chemical testing is expensive and time consuming. It is hypothesized that changes to the electrical properties of feed powder from reuse offers a pathway to in-line monitoring of feed powder quality. As a first step to developing an electromagnetic nondestructive evaluation method, broadband dielectric spectroscopy (BDS) measurements of wax-based metal powder composites were conducted. Seven different stainless-steel powder samples were prepared by altering their PSD, morphology and surface chemistry. It was shown that changes in PSD, morphology, and surface chemistry could be detected using BDS. These results will aid in the development of an in-line capacitive sensor for monitoring feed powder quality.

CHAPTER 1. INTRODUCTION

This research explores the application of broadband dielectric spectroscopy to detect changes in additive manufacturing feed powder. The feed powder used in additive manufacturing is affected by the high temperature build process which causes changes in the powder morphology, particle size distribution, and surface oxide. These changes may affect the electric permittivity of the powder which can be detected using broadband dielectric spectroscopy.

1.1 General introduction

Additive manufacturing of metal parts is a new and rapidly growing industry. The process of additive manufacturing, where a part is built in incremental layers, was pioneered in the late 1980s at the University of Texas at Austin by J. J. Beaman and C. R. Deckard (1). Following the first selective laser sintering (SLS) system patent in 1990 by Deckard and Beaman, additive manufacturing has experienced an explosion of innovation and research interest, especially industrial additive manufacturing. One of the largest exhibitions and conferences for industrial additive manufacturing, Formnext, had over 850 industrial exhibitors in attendance in 2019 (2). There are many technologies in use and being developed for metal additive manufacturing. These different laser based technologies have been broadly classified by Gu into three categories: laser sintering (LS), laser melting (LM), and laser metal deposition (LMD) (3). In addition to a laser heat source, some additive manufacturing systems use an electron beam heat source. Laser sintering uses the laser heat source to partially melt and fuse feed powder together. Typically, the feed powder is a mixture of metal alloys or a premixed alloy. The mixture of powders allows for a high melting point structural component and a low melting point binder (3). Laser melting based systems use a laser heat source, which is more powerful than that used in laser sintering, to fully melt the feed powder. Melting the feed powder creates a fully dense final product with density approaching

99.9% (3). Whereas, the density of laser sintered parts has been measured at 95% following post processing binder removal and infiltration of a filler metal (4). In both laser sintering and laser melting the apparatus is functionally the same; a flat layer of powder is held in a powder bed over which the laser source is scanned to either sinter or melt the feed powder. Whereas, in laser metal deposition the feed stock in the form of powder or wire is injected into the laser path where it is melted and deposited onto the part (3). This research concentrates on the additive manufacturing feed powder used, independent of the melting method. For simplicity, I will reference the laser based powder bed fusion system throughout this thesis. Laser melting is sometimes called powder bed fusion. In a powder bed fusion system, the part is built layer by layer. First, feed powder is spread in a thin flat layer in the powder bed. Next, the heat source is scanned across the XY plane of the feed powder melting and fusing the powder into a solid. This process continues layer by layer until the part is finished. Most of the feed powder placed into the powder bed is not fused into a final product and is recycled back into the system for future use. Reuse of feed powder is a major advantage of additive manufacturing because it reduces the material costs of production, but it is also a source of problems, as described in the next paragraph.

In a powder bed fusion system there are many process parameters under control of the operator such as: laser power, the output power of the laser; hatch distance, the lateral displacement between linear laser traces; scanning speed, the translational velocity of the part or laser beam; and layer thickness, the thickness of the feed powder layer in the powder bed (5). These parameters act to control the heat flow into the material to create a homogeneous, fully dense part (3). Incorrectly setting these parameters can yield poor quality parts which exhibit porosity defects such as gas entrapment or lack of fusion, which may result in inconsistent build quality (5). In laser melting systems gas entrapment can occur from two main sources, gas present in the feed powder and shielding gas entrapped by the Marangoni effect (5). The Marangoni effect is the mass transfer which occurs between two fluids with a surface tension gradient (6; 5). Lack-of-fusion defects occur when there is not enough thermal energy to melt the feed powder (5). Aside from trial and error or operator experience, there is little information available to the technician for initially setting these

parameters, and once set the operators typically refrain from adjusting them. Process parameter optimization is an active area of research for various engineering materials. Many researchers approach the question by measuring the mechanical properties of the built parts as the process parameters are varied. This approach results in a collection of parameter values which seem to work best for a given material (7; 8; 9). However, as the feed powder is recycled through multiple build cycles the build quality degrades while using the same process parameters. This degradation can be attributed to changes in the feed powder properties over multiple build cycles which mean that the initial process parameter settings become sub-optimal.

Multiple research groups and equipment manufacturers have used mechanical and chemical characterization techniques to investigate the change in feed powder properties over multiple build cycles (10; 11; 12). With regard to stainless steel alloy 316L feed powder, the material studied herein, the literature shows that there is an increase, over build cycles, in the average particle diameter and the oxygen content of the feed powder (12; 11; 13; 14). The change in the particle size distribution is attributed to a reduction in fines (particles with diameters less than the mean diameter) with an increase in the number of larger particles. Smaller particles are removed during the additive manufacturing process by sintering into larger particles (10; 5). Large and irregularly shaped particles can be created during the build process by the agglomeration of weld splatter from the melt pool, partial sintering, and lack of fusion processes (5). Increasing oxygen content in the feed powder has been associated with an increase in the thickness of the oxide layer of the un-melted feed powder (11). These cited works employed sophisticated and costly mechanical and chemical characterization tools to gather data on the feed powder. It may be possible, instead, to use the electrical properties of the powder to determine process parameters or the fitness for use of the feed powder.

In this study we seek to assess the feasibility of using the electrical properties of the metal feed powder to characterize the overall quality of the feed powder for use in additive manufacturing. Measurement of the electrical properties can be faster, less expensive, and importantly nondestructive, when compared to mechanical means of testing. To capture the possible changes in the feed

powder during a build cycle, seven different stainless steel 316L powder samples were prepared by altering their particle size distributions, morphology, and oxygen content. Broadband dielectric spectroscopy was employed to investigate the electrical properties of wax-based composites formed with dispersed samples of the metal powder. This work potentially supports the development of nondestructive evaluation techniques which can characterize the feed powder properties and provide in-line production feedback. This feedback can close the production loop allowing timely and intelligent setting of process parameters which affect build quality.

1.2 Dissertation organization

This thesis is laid out in three chapters. Chapter one includes a general introduction of additive manufacturing and the systems currently in use while identifying the challenges encountered during feed powder reuse. Additionally, the background topics which are used to develop and support my hypothesis are discussed: dielectric relaxation in solids, broadband dielectric spectroscopy, and effective medium approaches. Lastly, the major hypothesis and research statement are presented. Chapter two discusses in detail the study materials, sample preparation, and experimental method. The thesis concludes with the third chapter wherein the results are discussed, conclusions drawn, and suggestions for future work and applications are given.

1.3 Background and literature review

Broadband dielectric spectroscopy (BDS) is a powerful analysis tool based on measuring the complex impedance $Z(\omega)$ of a material in the frequency range of 10^{-6} Hz to 10^{12} Hz (15). By analyzing how the impedance changes with frequency (ω), electrical properties of the material can be determined. Additionally, because the change in the material's behavior with frequency is related to the structure of the material, the spectra can contain information about the physical and electronic structure of the material. Broadband dielectric spectroscopy measures the macroscopic bulk properties of a material; which treats the material as a homogeneous isotropic medium. This treatment means that the results can be directly applied to homogeneous isotropic materials.

Whereas, in the case of inhomogeneous materials such as composites, it is necessary to use effective medium theories or some other method to interpret the results. Several effective medium theories have been developed to predict the effective electrical properties of a mixture of materials. I will discuss a fundamental overview of the broadband dielectric spectroscopy measurement technique, dielectric relaxation in solids, and finally several effective medium theories used to predict the electrical properties of mixtures or composites.

1.3.1 Dielectric relaxation in solids

In the previous section I discussed how broadband dielectric spectroscopy is typically performed. This section is concerned with why the complex permittivity changes with frequency. Jonscher (16) defines relaxation from a mechanical point of view as, "the recovery of strain on removal of stress." We see this type of behavior when we press and remove our hands from a foam mattress. The hand print deformation slowly returns to normal. Relaxation is not instantaneous because all physical systems have "inertia" whether it be physical inertia from the mass of molecules, or the electrical force of interaction between a charge carrier and the material lattice. In dielectric relaxation, and other dielectric measurement techniques (dielectric resonance), we are concerned with how the polarization within the material changes upon the removal of an external electric field.

Polarization ($\overrightarrow{P}$) is a vector quantity defined as the dipole moment ($\overrightarrow{p}$) per unit volume. Revisiting the constitutive equation for displacement, $\overrightarrow{D} = \epsilon_0 \overrightarrow{E} + \overrightarrow{P}$, we see that the displacement is composed of two parts, the free space response $\epsilon_0 \overrightarrow{E}$ and the material response $\overrightarrow{P}$, giving the units for polarization as Coulombs per unit area. Dipoles are formed by the finite separation of positive and negative charges within a material, giving rise to a dipole moment $\overrightarrow{p} = qd\hat{d}$ which is a vector quantity pointing along the charge separation from the negative charge to the positive charge with magnitude equal to the amount of charge q separated by a distance d. Polarization is then the vector sum of the dipole moments per unit volume. Dipoles can be permanent such as the charge separation which occurs in molecular bonds (polar molecules such as water), or induced as the material responds to the applied electric field (molecules which are stretched by an electric field

form dipoles which oppose the stretching) (17). An intermediate polarization mechanism between the permanent dipoles and the induced dipoles is polarization by hopping charge carriers. Jonscher in (17) describes polarization by hopping charge carriers as the movement of electric charge between localized sites in the material. As an example, Jonscher describes a crystalline solid composed of a lattice of NiO. If one of the Ni++ atoms is replaced with a monovalent lithium atom Li+, the lithium site looks negative in comparison to the nickel sites. To restore charge neutrality a nearby Ni++ atom will give an electron to the Li+ atom, creating a Ni+++ atom and a dipole moment pointing from the Li site to the Ni+++. The electron can come from any nearby Ni++, therefore the positive charge associated with the Ni+++ can hop between energetically favorable Ni++ sites (17). Which site is energetically favorable is influenced by the application of an electric field. Jonscher further points out that if, in strongly disordered materials such as amorphous and non-metallic solids, there exists a linking network of localized defect sites that span the dimensions of the material then the movement of the hopping electrons through the material would be indistinguishable from direct current conduction (17). Therefore, the phenomena responsible for the formation of dipole moments can also lead to direct current conduction in amorphous solids where band conduction via free charge carriers does not typically occur (17). Jonscher further points out that materials which exhibit charge hopping polarization have alternating current conductivity which can be modeled by $\sigma'(\omega) = \sigma_0 + A\omega^n$ (17). When plotting the real part of the complex conductivity for these systems, two regimes of power law behavior become apparent as shown in Figure 1.1. A low frequency regime where the conductivity approaches the DC asymptote σ_0 and a high frequency regime where the conductivity becomes linear in the log of frequency, the transition between the two behaviors is marked by a transition frequency ω_c which is proportional to the DC conductivity σ_0 according to the Barton-Nakajima-Namikawa (BNN) relationship (15). The transition between the low frequency regime and the high frequency regime is related to the long range and short range mobility of the hopping carrier. In the low frequency regime the conductivity is limited by the long range mobility; whereas, in the high frequency regime the conductivity is limited by short range mobility. Kremer points out that the transition frequency marks the "bottle neck" in the charge

carrier system after which the conductivity saturates as frequency is lowered (15). In a percolating network this bottle neck may be the most energetically difficult or unlikely hopping transition.

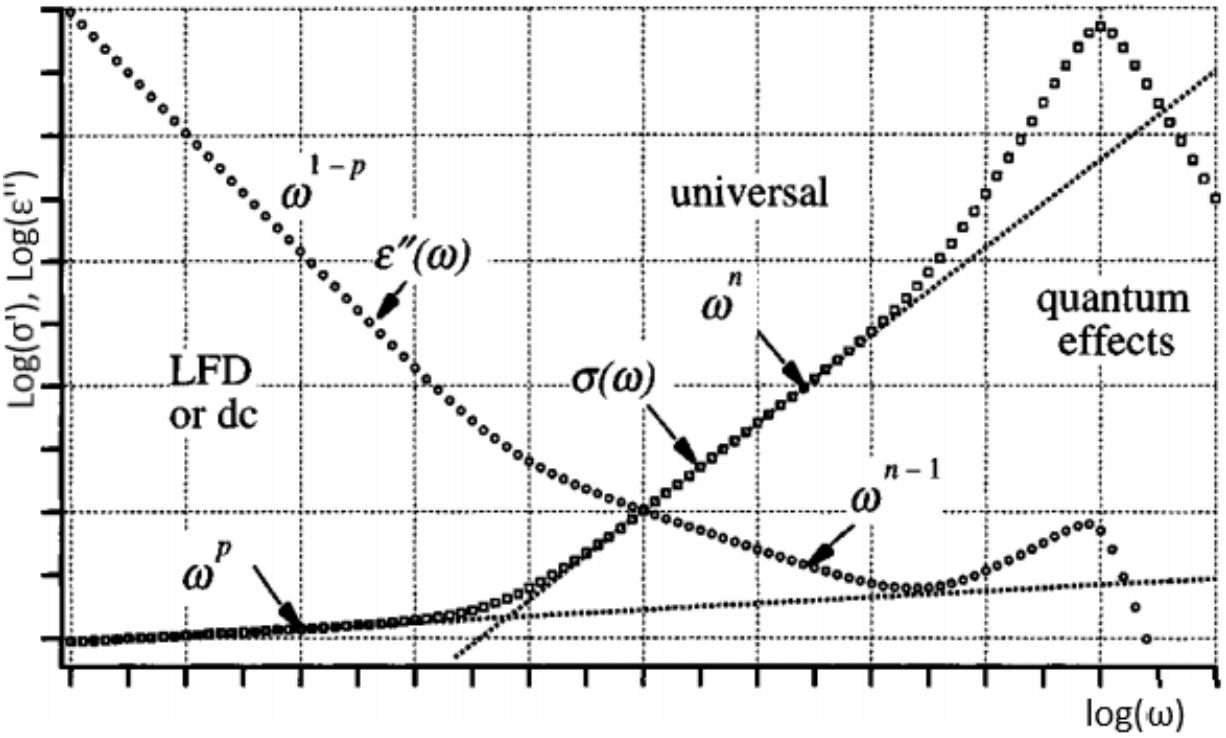

Figure 1.1 Representation of a hopping carrier system showing relationship between the log of the real part of the complex conductivity $\sigma'(\omega)$ and the log of angular frequency (ω). Source: Adapted from (16)

Having discussed the formation of electric dipoles in some materials, we will now continue to describe the dispersive behavior of permittivity, or polarization, with frequency. An electric dipole in an electric field experiences a torque that attempts to align the dipole with the external electric field. This is easiest to envision for dilute solutions of non-interacting polar molecules such as those studied by Debye (18). When the electric field is applied to the solution of polar molecules, which are free to move, they rotate to align their dipole moments with the field. In the static case, Debye only considered the randomizing influence of thermal agitation which competes with the ordering influence of the applied field to calculate the average dipole moment for the dilute solution (17).

In the transient case, Debye further considered the viscosity of the fluid in which the dipoles are floating to be the limiting factor which could prevent full alignment of the dipole moments with the applied field. With respect to the transient case with a sinusoidal electric field, Debye noted in (18) that because the dipoles require a finite time to align themselves, eventually as the frequency of oscillation increases, "one quarter of a period of the electrical force will be insufficient time for the molecules to orient themselves." The inability of the molecules to follow the electric field as frequency increases causes an overall reduction in the polarization from the static case; which is the dispersion of permittivity with frequency. This phenomena occurs in all materials including materials which exhibit charge hopping (17). Dispersion of permittivity in charge hopping systems is affected by the transition probabilities between localized hopping sites (17). In other words, the electric field could oscillate faster than the transition probability would allow for the electron to execute a hop. In which case, the hopping mechanism no longer contributes to the overall polarization.

1.3.2 Broadband dielectric spectroscopy: A fundamental overview

The frequency-dependent electrical properties of materials are of practical interest to both engineers and solid state physicists. Electrical engineers need to select materials whose behaviors will be stable and predictable within their operating environment while physicists are concerned with the underlying mechanisms causing the dispersion in the material property with frequency. Starting with the engineers perspective, this section will discuss how broadband dielectric spectroscopy measurements are conducted.

The dielectric data can be represented in various equivalent forms. However, the primary electrical property of interest when discussing dielectrics is their complex permittivity $\epsilon^*(\omega) = \epsilon'(\omega) - j\epsilon''(\omega)$, ($\omega$ is the radial frequency, $j = \sqrt{-1}$). The real part of the complex permittivity $\epsilon'(\omega)$ is proportional to the energy stored (or polarizability) of the external excitation and the imaginary part of the complex permittivity $\epsilon''(\omega)$ is proportional to the energy lost per period (15). The complex permittivity is a function of frequency or time because of the inability of a system

to instantaneously respond to the change in an external excitation, as discussed in Section 1.3.1. From the constitutive relation for electrical displacement $\overrightarrow{D} = \epsilon^* \epsilon_0 \overrightarrow{E}$ (where $\overrightarrow{D}$ is the displacement or surface charge developed on the dielectric when exposed to an external electric field $\overrightarrow{E}$, and ϵ_0 is the permittivity of free space) it can be seen that ϵ^* affects the amplitude and phase of the material response to an external field. A common way to measure the permittivity of a material is to form a parallel plate capacitor with the material as in Figure 1.2. The resulting capacitance can be calculated using the simple relation for an ideal parallel plate capacitor $C^* = \epsilon^* \epsilon_0 \frac{A}{d}$ (where A is the area of the electrode and d is the separation between the electrodes). The impedance of the parallel plate capacitor can then be measured and the capacitance determined from the relation $Z^*(\omega) = \frac{-j}{\omega C^*}$ (where $Z^*(\omega)$ is the frequency dependent impedance, it is understood that $Z^*(\omega)$ is a frequency dependent complex value and typically it is represented only as Z). Impedance is the sinusoidal analog to Ohm's law $V = IR \rightarrow |V| \angle \theta_v = |I| \angle \theta_I Z$, where now the voltage and current are phasor quantities with magnitude and phase angle. The impedance of the parallel plate capacitor is measured as shown in Figure 1.3. A sinusoidal excitation voltage is applied across the capacitor and the resulting current through the capacitor is measured. Modern instruments such as the Novocontrol Alpha-A use digital lock-in amplifiers to increase the signal to noise ratio and precision transimpedance amplifiers to accurately measure the current signal. A dielectric spectrum, such as that shown in Figure 1.4, is gathered by measuring the impedance as the frequency is swept in the range of μHz to GHz.

1.3.3 Effective medium approaches

Effective medium theories try to model the effective or overall properties of inhomogeneous media by taking into account the material parameters, volume fractions, size and shape distributions, etc, of the constituent materials. Kremer points out in (15) that James Clerk Maxwell was the first to derive a mean field theory for a composite made of dispersed spherical particles in a matrix material which he wrote about in his 1873 treatise on electricity and magnetism (20). In a section titled *conduction in heterogeneous media*, Maxwell describes a process to calculate the

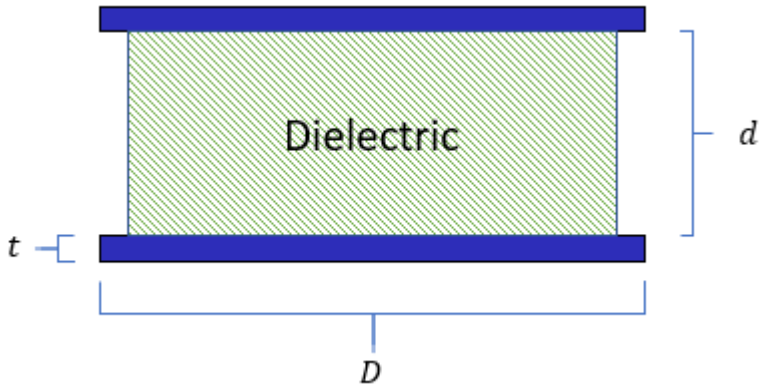

Figure 1.2 Schematic of a cylindrical parallel plate capacitor incorporating a dielectric between the two cylindrical electrodes (shown in blue). D is the electrode diameter, d is the separation between the electrodes, and t is the electrode thickness.

static effective resistivity ρ of a spherical matrix which contains spherical inclusions. Maxwell's effective medium theory was based on the assumption that the spherical inclusions are remote from each other such that the perturbation on the incident current density by each spherical inclusion was independent. In other words, the potential for each spherical inclusion uses the same form independent of where the inclusion is located. Additionally, Maxwell only considered real valued electrical properties in his derivation. Another important relationship that Maxwell noted in his treatise was how the behavior of a stratified dielectric composed of layers of material with different electrical properties can exhibit dielectric relaxation even though the constituent materials may be ideal, loss-less dielectrics. This phenomenon is referred to as interfacial polarization and was further developed by Wagner (21) and Sillars (22). Later in 1904 James Clerk Maxwell-Garnett developed a quasi-static theory which incorporated the Lorentz local field approximation to model the dipole-dipole interactions between spherical particle inclusions in a matrix (23). The Maxwell-Garnett formula can be written as follows (23).

$$\frac{N'^2 - \nu^2}{N'^2 + 2\nu^2} = \varphi_f \frac{N^2 - \nu^2}{N^2 + 2\nu^2} \tag{1.1}$$

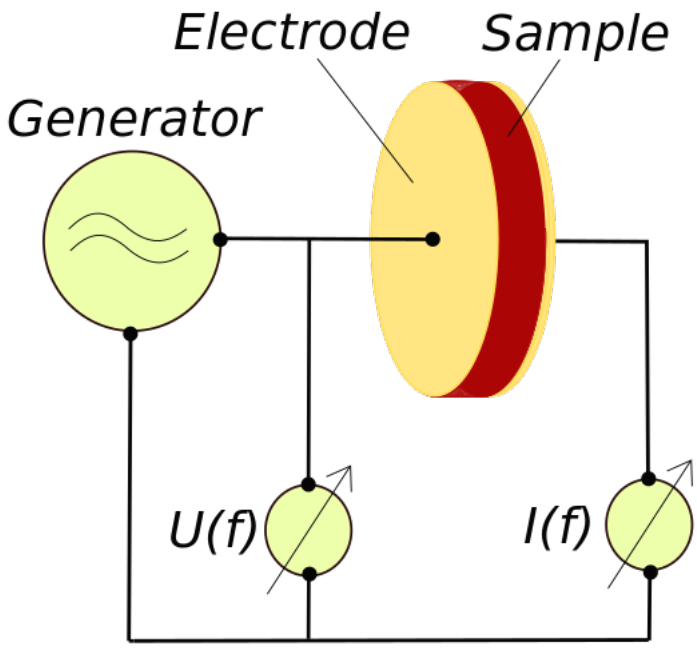

Figure 1.3 Schematic of a typical impedance measurement setup showing the sinusoidal excitation source and the measurement of the voltage $U(f)$ and current $I(f)$ through the parallel plate capacitor. Source: Adapted from (19)

In the preceding equation φ_f is the volume fraction of the inclusion, N' and N are the optical constants ($N = \sqrt{\epsilon^*}$) for the effective medium and the inclusion respectively, and ν is the refractive index of the matrix, $\nu(1-i\kappa) = \sqrt{\epsilon^*}$, where κ is the absorption coefficient for the material. Maxwell-Garnett was interested in modeling the colors of metal glasses and using his theory he was able to predict the colors of glasses based upon the optical properties of the mixture components (23). The Maxwell-Garnett formula is applicable to dilute inclusion mixtures with volume fractions less than 20 percent and the size of the particles must be much smaller than the wavelength of the incident electric field such that the field can be approximated as uniform (15). In Maxwell-Garnett's work the volume fraction was on the order of 10^{-6} to 10^{-4} (23). Additionally, Maxwell-Garnett's model uses a lossless matrix material. In a parallel effort Wagner, in 1914, arrived at a similar expression while working to apply Maxwell's stratified dielectric ideas to a matrix particle system and create

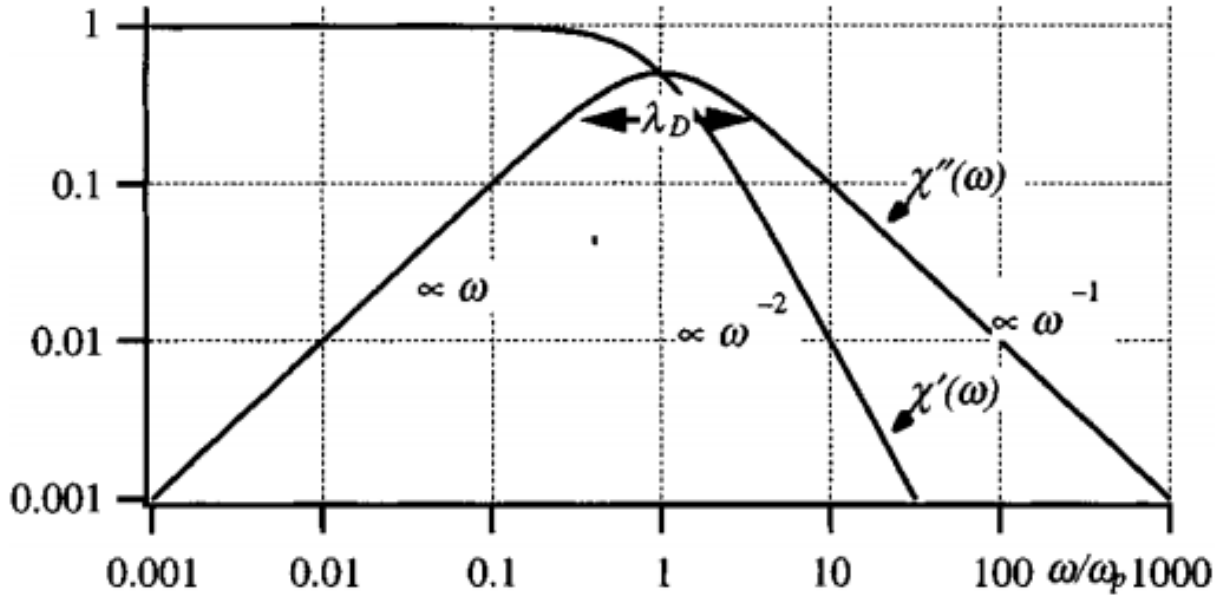

Figure 1.4 The real and imaginary part of the dielectric susceptibility for an ideal Debye process [Note $\epsilon^*(\omega) = 1 + \chi'(\omega) - j\chi''(\omega)$] . Source: Adapted from (16)

a more general theory (21). Wagner allowed for complex-valued electric properties in his theory to capture the effects of non-ideal dielectrics (15). Later in 1937, Sillars extended Wagners work to include ellipsoids by incorporating a shape factor which describes the orientation of the particles with respect to the axis of the applied field (22). Maxwell-Wagner-Sillars or MWS polarization can be calculated using the following relationships as set out by Kremer (15).

$$\epsilon_c^*(\omega) = \epsilon_m^*(\omega)\frac{n\epsilon_f^*(\omega) + (1-n)\epsilon_m^*(\omega) + (1-n)[\epsilon_f^*(\omega) - \epsilon_m^*(\omega)]\varphi_f}{n\epsilon_f^*(\omega) + (1-n)\epsilon_m^*(\omega) - n[\epsilon_f^*(\omega) - \epsilon_m^*(\omega)]\varphi_f} \tag{1.2}$$

$$n_a = \frac{4}{3}\pi abc\int_0^\infty \frac{d\xi}{(\xi + a^2)V(\xi)} \tag{1.3}$$

$$V(\xi) = \frac{4}{3}\pi\sqrt{(\xi + a^2)(\xi + b^2)(\xi + c^2)} \tag{1.4}$$

In the proceeding expressions, $\epsilon_m^*(\omega)$ and $\epsilon_f^*(\omega)$ are the complex permittivities of the matrix material and the filler material respectively. $\epsilon_c^*(\omega)$ is the complex permittivity of the effective media. φ_f is the volume fraction of the filler material. n_a is the shape parameter which describes the impact of

the particle shape. The shape parameter coincides with the axes of the ellipsoid named a, b, and c by Sillars. Sillars studied the effect of prolate and oblate spheroids (22). In Sillars' derivation the a axis points along the applied field axis, n can take on values between $0 \leq n \leq 1$, and for a sphere $n = \frac{1}{3}$. The effect of changing the particle shape can be seen in Figure 1.5. This figure is representative of water droplets suspended in paraffin wax. As the water droplets are elongated in the direction of the field, the amount of water necessary to reach the desired loss factor ($\tan\delta = \frac{\epsilon''}{\epsilon'}$) decreases and the frequency at which the maximum loss factor occurs decreases (22). Therefore, in systems with the same volume fraction of material, we would expect much higher losses as the inclusions are elongated. It can be shown that the MWS formula reduces to the Maxwell Garnett formula for spherical inclusions where the matrix material has frequency independent permittivity with no conductivity and the inclusion material has frequency independent permittivity and conductivity.

In summary, heterogenenous materials such as composites where there is a contrast in material properties give rise to interfacial polarization and dielectric relaxation. Interfacial polarization is affected by the material property contrast between the matrix and inclusion materials, the volume fraction of the inclusions, the shape of the inclusions, the spatial distribution of the inclusions, the orientation of the inclusions with respect to the applied field, and the size distribution of the inclusions.

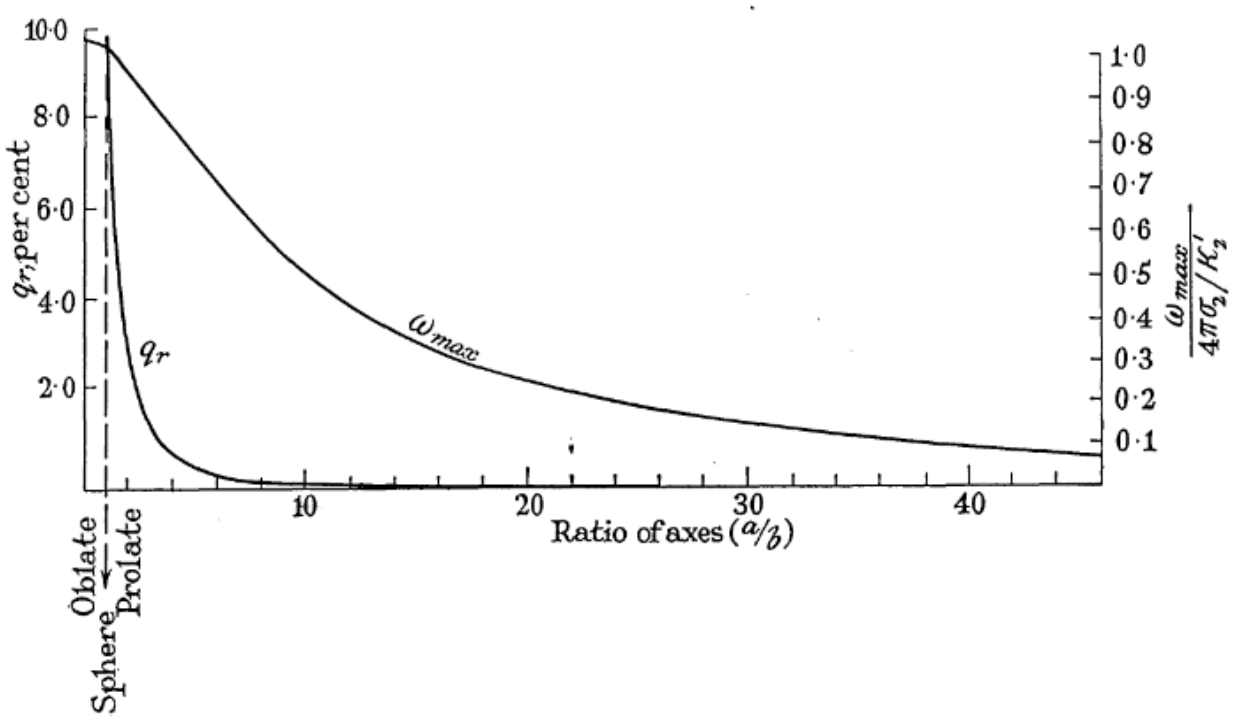

Figure 1.5 Predicted volume percent q_r of conductive filler to produce a maximum $\tan\delta = 0.01$ for $\epsilon_f' = 41\epsilon_m'$, as a function of the axis ratio a/b of spheroidal inclusions whose a axis are aligned with the external field. Source: Adapted from (22)

1.4 Hypothesis

Feed powder particles used in powder bed fusion systems undergo changes in morphology, particle size distribution, and surface oxidation during the additive manufacturing build process. I hypothesize that these changes to the powder will cause a change in the powder's electrical permittivity which can be detected using broadband dielectric spectroscopy, this change in permittivity can be used as the basis for the development of an online capactive nondestructive evaluation method in order to monitor the changes in the feed powder through build cycles.

CHAPTER 2. EXPERIMENTAL

The following sections detail the experimental materials used, the measurement methods, and the procedures used to prepare data for analysis.

2.1 Study materials and preparation

Seven 316L stainless steel powders were provided by the Naval Nuclear Laboratory (NNL) for use in this study. The powders were purchased from AMTEK, a commercial supplier of additive manufacturing metal powders. All powders were used as supplied. The powders have been designated M316L1 through M316L5, and the two oxidized powders have been designated NNL1 and NNL2. M316L1 through M316L5 have been modified by the manufacturer to change the particle size distribution and morphology of the particles. NNL1 and NNL2, have been intentionally oxidized to develop or grow the oxide layer on the surface of the powder. M316L1, M316L4, M316L5 have been manufactured using gas atomization; whereas, M316L2 and M316L3 have been manufactured using water atomization. Water atomization creates a more irregular non-spherical particle than gas atomization; which can be seen in Figure 2.1. The differences between the powders is summarized in Table 2.1. Additionally, paraffin wax (411663-1Kg) was supplied from Sigma Aldrich and used as received. The paraffin wax was used as a binder for making dielectric spectroscopy samples; which will be discussed in a following paragraph.

Table 2.1 Designed property variations, manufacturer provided size information, and measured density results. The size information from the manufacturer represents: (mesh screen through which the powder passes/mesh screen through which the powder does not pass).

Powder	**Manufacturing Method**	**Size** (μm)	**Density** (g/mL)	**Notes**
M316L1	Gas atomized	(74/10)	7.83 ± 0.02	wide distribution
M316L2	Water atomized	(63/20)	7.83 ± 0.02	most irregular shape
M316L3	Water atomized	(63/20)	7.74 ± 0.02	more spherical shape
M316L4	Gas atomized	(74/25)	7.88 ± 0.02	fines depleted
M316L5	Gas atomized	(88/10)	7.88 ± 0.02	bimodal distribution
NNL1	Gas atomized	note	7.87 ± 0.02	oxidized 0.25%
NNL2	Gas atomized	note	7.84 ± 0.02	oxidized 0.35%

Note: The size information for powders NNL1 and NNL2 was not available at the time of writing.

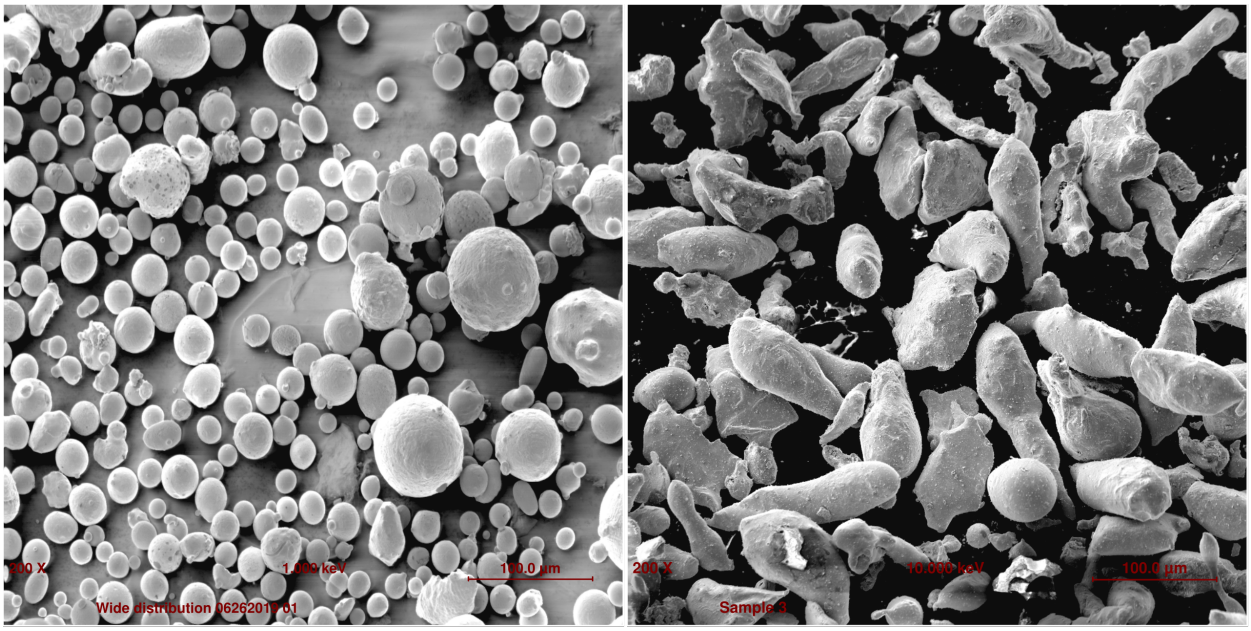

Figure 2.1 Secondary electron micrographs showing the difference in morphology between gas atomized (left) and water atomized (right) powders. Note the prolate spheroidal shape of the water atomized powder. Secondary electron microscopy performed by Michael Burrell (NNL)

2.1.1 Material characterization

The particle size (diameter in microns) distribution of powders M316L1-M316L5 were analyzed using histogram plots and by fitting a log normal cumulative distribution function to the cumulative percent undersize calculated from the sieve analysis provided by the manufacturer. The cumulative percent undersize was chosen so that the function increases monotonically as the mesh size in microns increases, whereas the cumulative percent mass increases monotonically as the mesh size in microns decreases. The fit was performed using the *nlinfit* function of MATLAB, with parameter estimates based on hand plots of the cumulative percent undersize on Weibull two cycle log paper, as described in (24). The results of the fit can be seen in Figure 2.3. The probability density function of the powder size was parameterized from the fit results and can be seen in Table 2.2. The skewness or asymmetry of the log normal probability distribution is a function of the σ fit parameter where skewness $= \left[\exp\left(\sigma^2\right) + 2\right] \sqrt{\exp\left(\sigma^2\right) - 1}$. Therefore, the wideness of the distribution is proportional to the standard deviation (σ) of the $\ln(x)$, where x is the particle diameter.

The density of the metal powders used in this study were measured using a helium pycnometer (G-DENPYC 2900). The measurement results are tabulated in Table 2.1. Each density value is the mean of ten repeated density measurements; the reported density is based on a standard uncertainty multiplied with a coverage factor $(k = 2)$, providing a level of confidence of approximately 95%. The uncertainty in the density measurement was determined in accordance with the International Organization for Standardization guide to the expression of the uncertainty in measurements (25).

Secondary electron images and size distribution estimates were made available by the researchers at Knolls Atomic Power Laboratory. These secondary electron images, in Figure 2.5 and 2.6, show the stark contrast in morphology between powders produced via gas atomization and water atomization. Additionally, the relative size distributions for the gas atomized powders can be seen in the images. The size distributions were estimated from scanning electron microscopy images. Size distribution results are provided for the oxidized powders NNL1 and NNL2 in Figure 2.4.

Table 2.2 Metal powders cumulative percent undersize log normal fit parameters and calculated expectation of the powders diameter. The reported uncertainty is the 95% confidence interval provided by the MATLAB fitting function

Powder	$E[\ln(X)]$, μ	Std$[\ln(X)]$, σ	$E(X)$, $\exp(\mu + \frac{\sigma^2}{2})$ (μm)
M316L1	3.7 ± 0.1	0.5 ± 0.2	50 ± 6
M316L2	3.44 ± 0.02	0.23 ± 0.03	32 ± 1
M316L3	3.6 ± 0.1	0.3 ± 0.2	40 ± 4
M316L4	3.89 ± 0.06	0.3 ± 0.1	50 ± 3
M316L5	3.8 ± 0.2	0.8 ± 0.4	60 ± 23

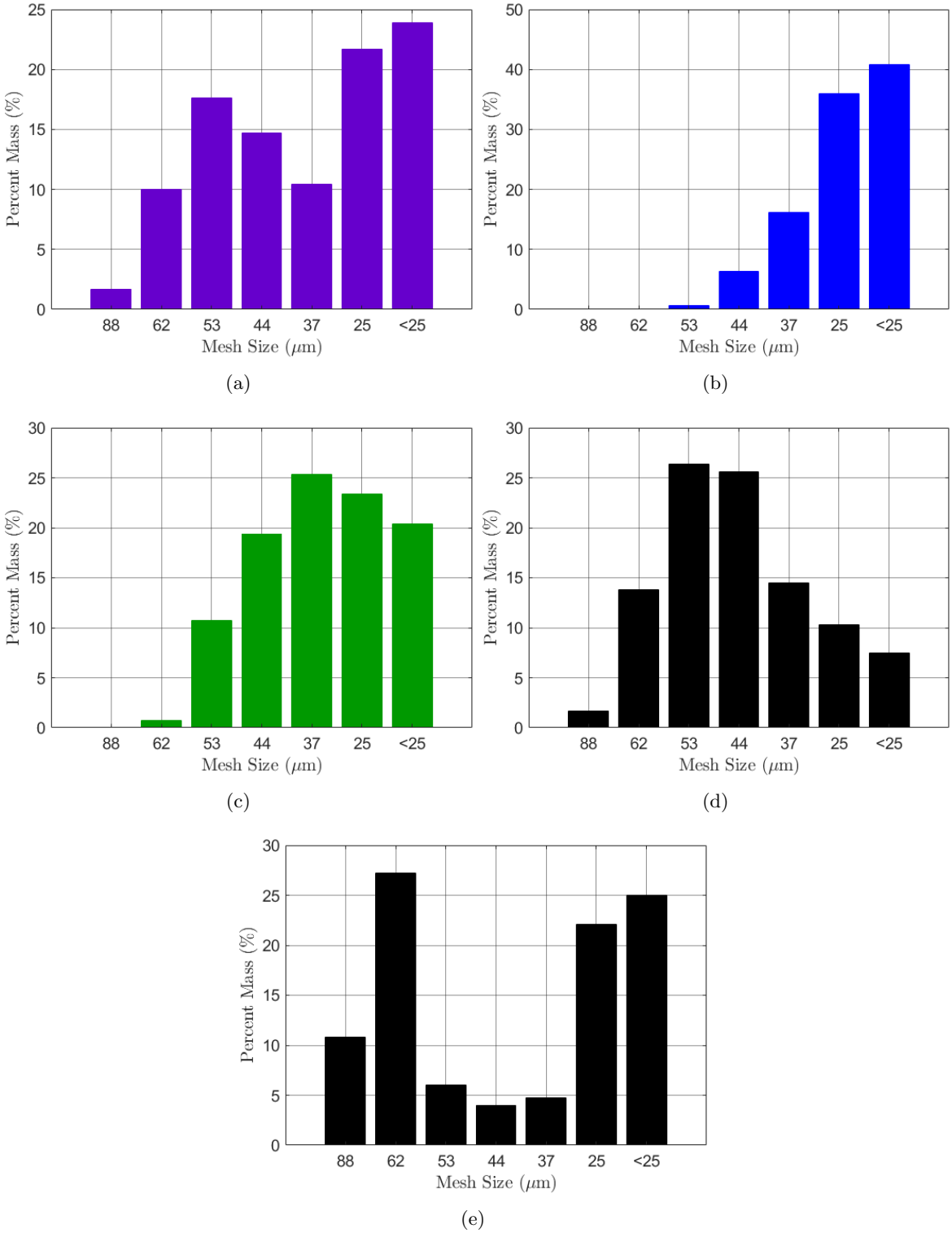

Figure 2.2 Histogram of manufacturer sieve analysis of metal powders showing percent mass of powder remaining on each sieve and percent mass of powder passing through to pan ($< 25\mu$m): (a) M316L1, (b) M316L2, (c) M316L3, (d) M316L4, and (e) M316L5

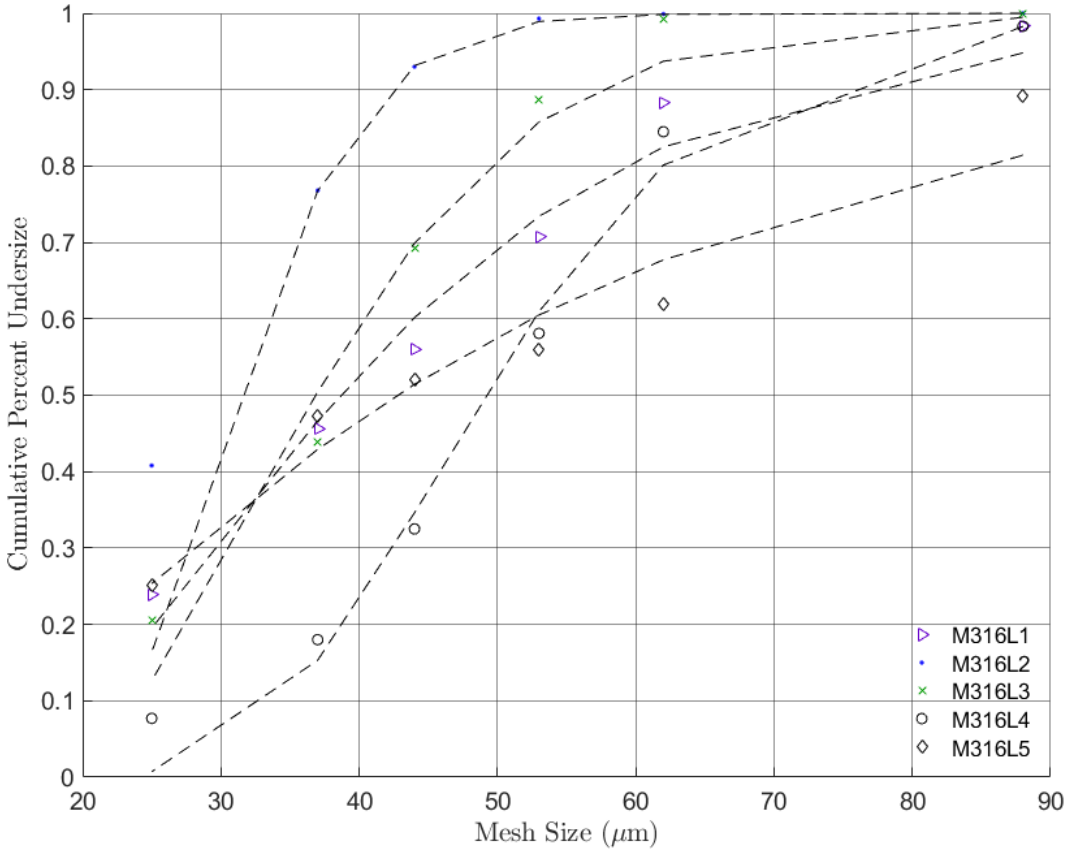

Figure 2.3 Comparison of the powders cumulative percent undersize, log normal model fits are shown as dashed lines.

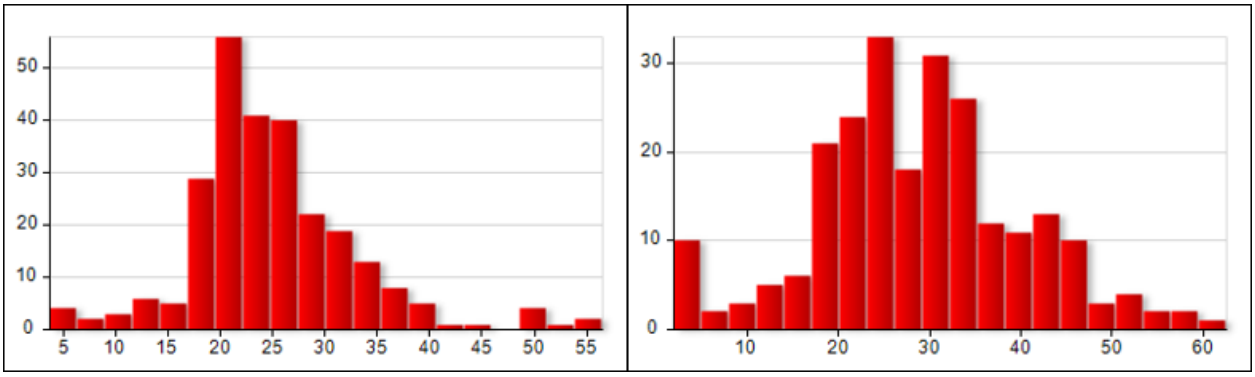

(a) (b)

Figure 2.4 Size distributions determined from scanning electron microscopy images: (a) NNL1, (b) NNL2. The vertical axis represents the particle count and the horizontal axis is the particle diameter in μm. Sizing information performed by Jessica Pyle (NNL)

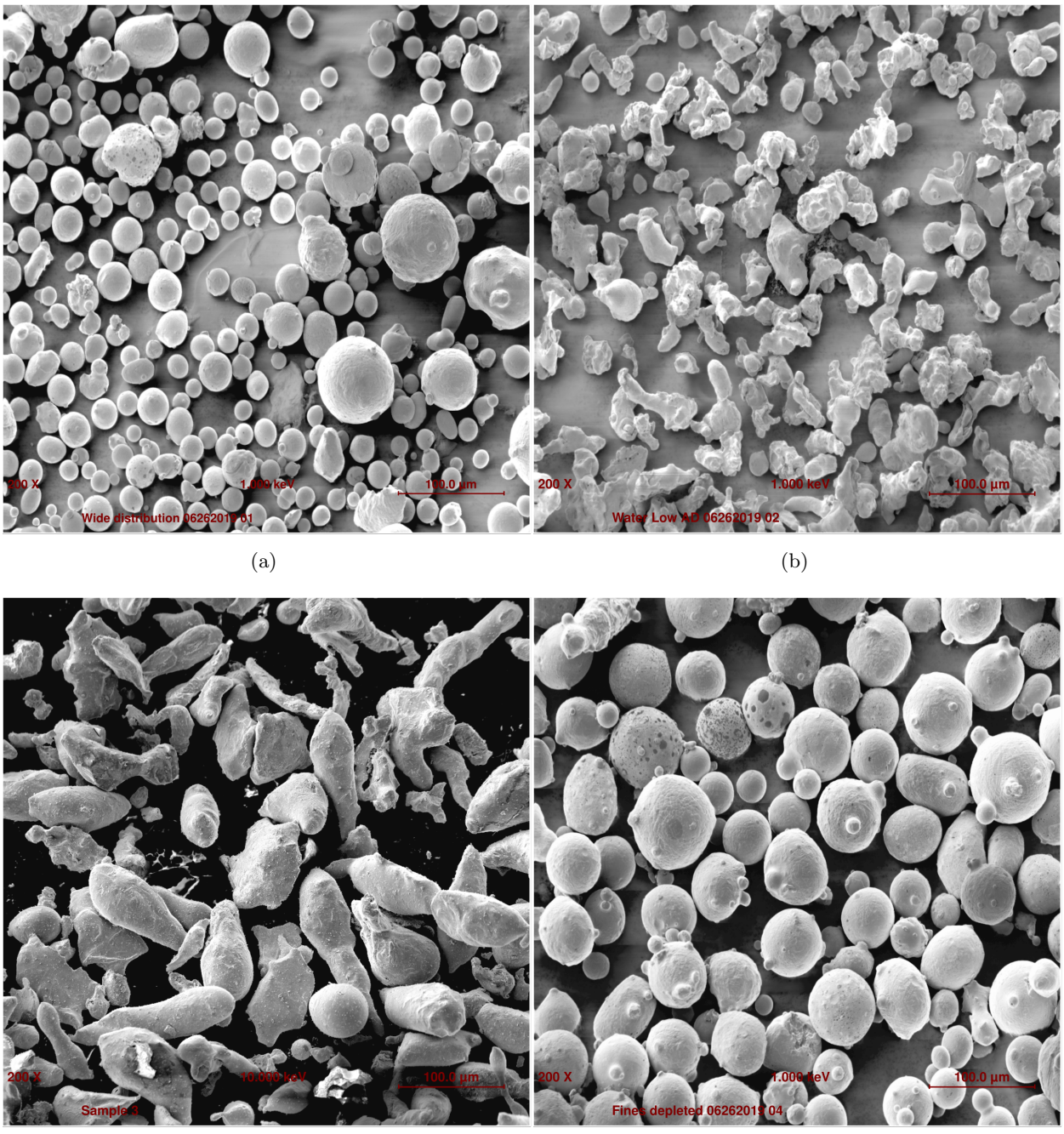

(a) (b)

(c) (d)

Figure 2.5 Secondary electron images: (a) M316L1, (b) M316L2, (c) M316L3, (d) M316L4. Secondary electron imaging performed by Michael Burrell (NNL)

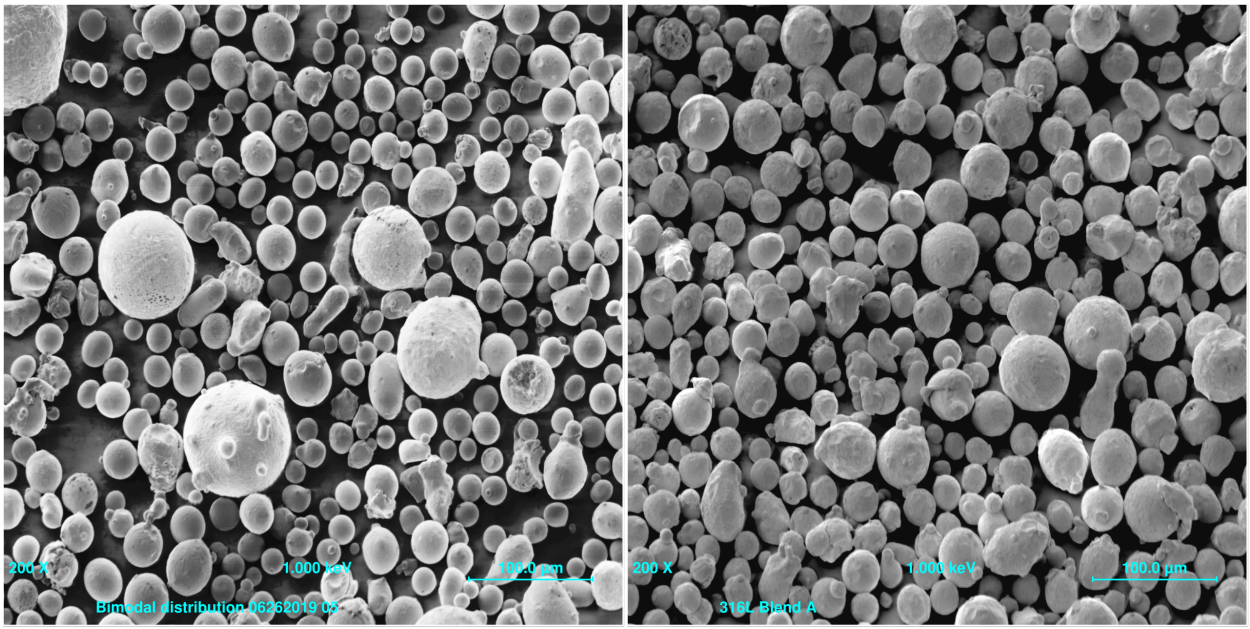

(a) (b)

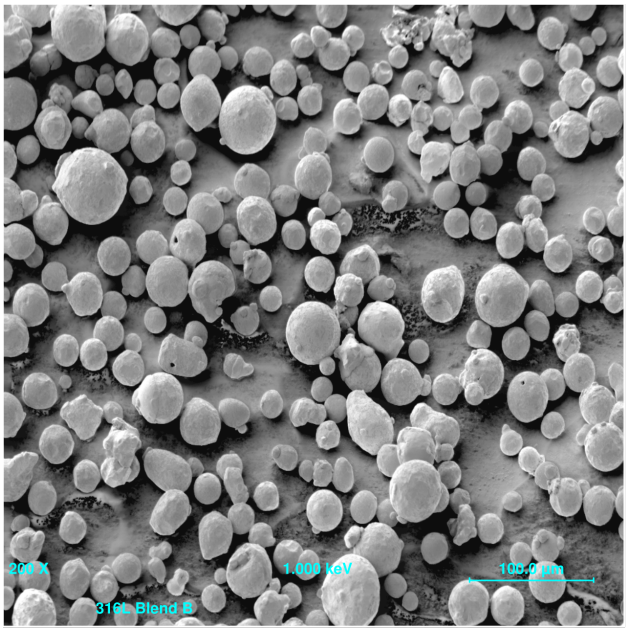

(c)

Figure 2.6 Secondary electron images: (a) M316L5, (b) NNL1, (c) NNL2. Secondary electron imaging performed by Michael Burrell (NNL)

2.1.2 Sample preparation

Thirty percent volume fraction metal powder composite samples (master batches) were formed by hand-blending the dry metal powder with melted paraffin wax. Resulting samples were 30:70 powder volume to volume of paraffin wax. Care was taken to fully incorporate and homogeneously distribute the metal powder. Thirty percent volume fraction samples were selected because the predicted permittivity of the various effective medium theories start to converge near 30 percent which gives the advantage that the results from the different theories can be directly compared. Additionally, it was found that at higher volume fractions the samples became too brittle for successful experiments. The volume fraction of the master batches was determined to be 0.32 ± 0.02; the reported uncertainty is based on a standard uncertainty multiplied with a coverage factor $k = 2$, providing a level of confidence of approximately 95%. The volume fraction was calculated assuming that the paraffin wax density, 0.89 ± 0.01 g/mL, was the average of the density ranges provided in (26). Additionally, the uncertainty in the paraffin wax density was taken to be uniformly distributed within the range of the handbook densities.

Spectroscopy samples were formed by pressing material from the prepared master batches in a 13-mm outer-diameter evacuable pellet die (Carver 3619), such as those used to form Fourier-transform infrared spectroscopy (FTIR) samples using potassium bromide powder. The master batch material was pressed in the die using a manual hydraulic benchtop press (Specac GS15011) set to three tons of pressure for three minutes. The time and pressure used were selected to create completely fused samples while limiting leakage of the paraffin wax through the small tolerance opening between the anvil and the die bore. The resulting pellet is a short cylinder with an outer diameter of 13 mm. The amount of master batch material was selected so that the finished pellet thickness would be approximately 0.5 mm, allowing for a capacitance measurement greater than 20 pF. The capacitance value of 20 pF was selected to ensure that the impedance measurement was in the most accurate region of the measurement equipment. To facilitate pellet removal from the die anvils a commercially available PDMA release agent was used. Comparisons in the dielectric spectroscopy results for pellets with release agent and pellets without release agent showed no

change in dielectric behavior within the frequency ranges measured. The use of the PDMA release agent and a cold plate allowed easy removal of the pressed pellets from the die anvils. The thickness of the spectroscopy pellets was measured using a digital indicator (Sylvac ultra mark IV 25 mm) and stand. To limit the deformation of the spectroscopy sample while measuring its thickness, the sample was sandwiched between two microscope slides of known thickness. The reported thickness is the mean of ten measurements across the surface of the sample. To account for and reduce the experimental error associated with sample variability ten replicate pressed samples from each master batch were made.

Following thickness measurements the electrode contact faces of the pressed samples were coated with a thin layer of colloidal silver paint. The silver paint reduces electrode contact resistance between the measurement equipment and the pressed sample, additionally the paint reduces the effect of air gaps from imperfect contact at the electrode to sample interface.

Table 2.3 Thickness measurements for the replicate pressed samples for each master batch. Each thickness value is the mean of ten measurements across the surface of the sample; the reported uncertainty is based on a standard uncertainty multiplied with a coverage factor $k = 2$, providing a level of confidence of approximately 95%.

Sample/ Powder	M316L1	M316L2	M316L3	M316L4	M316L5	NNL1	NNL2
A	0.688 ± 0.004	0.693 ± 0.003	0.714 ± 0.005	0.679 ± 0.005	0.692 ± 0.004	0.722 ± 0.005	0.719 ± 0.003
B	0.707 ± 0.005	0.698 ± 0.003	0.706 ± 0.003	0.691 ± 0.003	0.681 ± 0.005	0.710 ± 0.003	0.721 ± 0.004
C	0.701 ± 0.004	0.712 ± 0.005	0.714 ± 0.005	0.689 ± 0.004	0.698 ± 0.003	0.710 ± 0.005	0.728 ± 0.004
D	0.693 ± 0.003	0.725 ± 0.007	0.722 ± 0.004	0.674 ± 0.003	0.708 ± 0.004	0.712 ± 0.005	0.705 ± 0.004
E	0.704 ± 0.004	0.727 ± 0.003	0.692 ± 0.003	0.708 ± 0.003	0.719 ± 0.005	0.727 ± 0.005	0.702 ± 0.003
F	0.697 ± 0.004	0.707 ± 0.005	0.719 ± 0.003	0.689 ± 0.005	0.708 ± 0.004	0.723 ± 0.003	0.717 ± 0.003
G	0.704 ± 0.003	0.713 ± 0.003	0.718 ± 0.004	0.700 ± 0.004	0.703 ± 0.004	0.708 ± 0.006	0.713 ± 0.003
H	0.705 ± 0.004	0.698 ± 0.006	0.721 ± 0.004	0.699 ± 0.005	0.709 ± 0.004	0.713 ± 0.003	0.729 ± 0.004
I	0.699 ± 0.004	0.706 ± 0.003	0.696 ± 0.007	0.690 ± 0.004	0.687 ± 0.003	0.702 ± 0.003	0.728 ± 0.004
J	0.709 ± 0.004	0.701 ± 0.003	0.704 ± 0.005	0.692 ± 0.003	0.697 ± 0.003	0.714 ± 0.004	0.720 ± 0.003

2.2 Experimental method

The electrical properties of the metal powder composite samples were measured using broadband dielectric spectroscopy. Dielectric measurements were carried out using a Novocontrol Alpha-A dielectric/impedance measurement system consisting of the Novocontrol Alpha-A mainframe, ZGS Active sample cell shown in Figure 2.7, Quatro cryosystem, and desktop computer running the Novocontrol winDETA software. The complex capacitance of the pressed samples was measured using the following parameters: temperature maintained at 25.00 ± 0.01 °C, excitation voltage 1.00 ± 0.02 V_{rms}, frequency swept from 100 Hz to 10 MHz in 50 logrithmically spaced steps. Prior to gathering data, the equipment was calibrated and prepared for use in accordance with manufacturer procedures. Each pressed sample was measured ten times yielding 500 data points. The combined data for the ten replicate pressed samples gives 5000 data points for each metal powder composite.

The raw complex capacitance data from the Novocontrol system was post processed to correct for edge capacitance in accordance with (19). This additional nondispersive (the edge field moves through the air) capacitance is caused by the finite size of the electrodes. Corrections were necessary because of the small sample capacitances measured, the edge capacitance could account for nearly 20 percent of the measured capacitance. Following edge correction the complex conductivity and permittivity of the samples were extracted. These processes are discussed in more detail below.

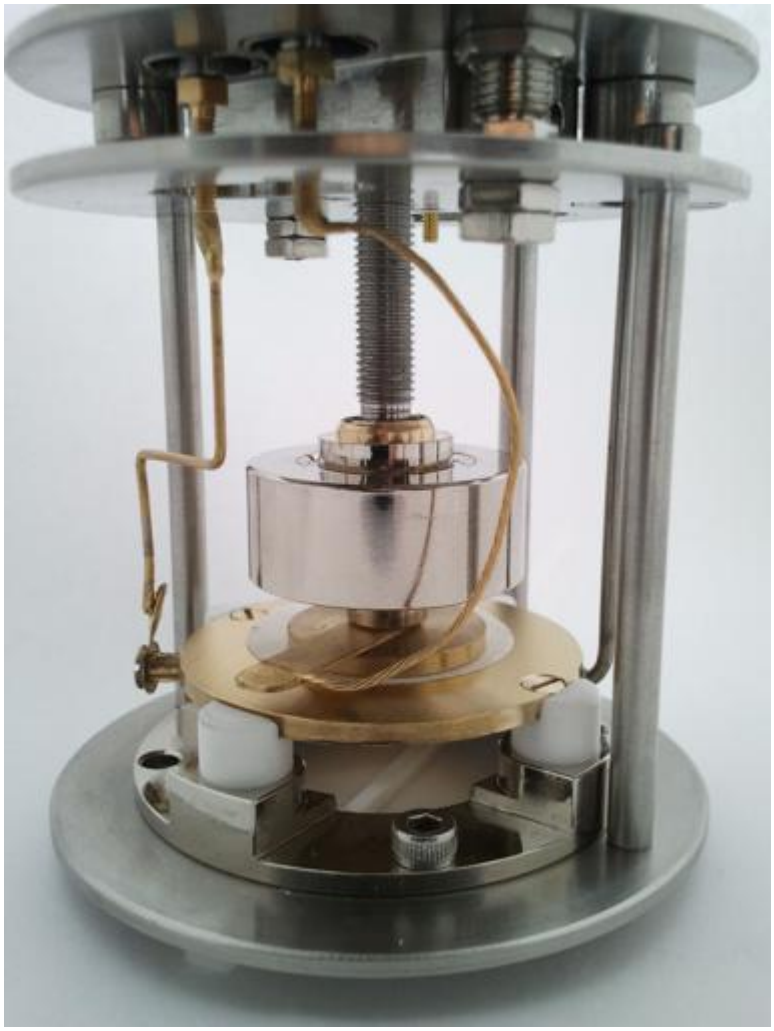

Figure 2.7 Novocontrol ZGS active sample cell showing the gold plated parallel plate electrodes. In the figure the upper electrode is separated from the lower electrode by a piece of white shipping material. The large silver colored cylinder above the upper electrode is an isolation mechanism between the electrode and the height adjustment screw. Source: (27)

2.2.1 Edge capacitance correction

Following calibration of the Novocontrol system the reference plane for the system extends to the built in electrodes of the ZGS active sample cell. The use of additional electrodes to form the sample capacitor adds uncompensated edge capacitance from the finite size of the additional electrodes. This uncompensated edge capacitance is in parallel with the sample capacitance and therefore, the edge capacitance adds to the sample capacitance. The uncompensated edge capacitance can be considered purely real, because the electric field extending from the edges of the electrodes passes through an approximately nondispersive medium, air. In the following equations C^*_{meas} is the measured capacitance, C^*_{samp} is the desired sample capacitance, C_{edge} is the undesired edge capacitance, δ is the angle between the real capacitance axis and the complex capacitance vector or $\frac{\pi}{2} - \theta$ where θ is the impedance phase angle, finally $j = \sqrt{-1}$.

$$C^*_{\text{meas}} = C^*_{\text{samp}} + C_{\text{edge}} \tag{2.1}$$

$$|C^*_{\text{meas}}| \cos(\delta) - j|C^*_{\text{meas}}| \sin(\delta) = C^*_{\text{samp}} + C_{\text{edge}} \tag{2.2}$$

Using the analytical expression for C_{edge} given in (19) and the above relationships C^*_{samp} can be determined.

$$C_{\text{edge}} = \epsilon_0 \frac{\pi}{4} \frac{D^2}{d} \frac{2d}{\pi D} \left[\ln \frac{8\pi D}{d} - 3 - z(x) \right] \tag{2.3}$$

$$z(x) = (1+x)\ln(1+x) - x\ln(x) \tag{2.4}$$

$$x = \frac{t}{d} \tag{2.5}$$

where D is the electrode diameter, d is the separation between electrodes, t is the electrode thickness, and ϵ_0 is the permittivity of free space. These dimensions can be seen in Figure 1.2.

2.2.2 Complex conductivity and permittivity extraction

Following edge correction, the complex permittivity $\epsilon^*(\omega) = \epsilon'(\omega) - j\epsilon''(\omega)$ was calculated from the sample capacitance C^*_{samp} using the parallel plate cylindrical capacitor relationship.

$$C^*_{\text{samp}} = \epsilon^* \epsilon_0 \frac{\pi}{4} \frac{D^2}{d} \tag{2.6}$$

The complex conductivity $\sigma^*(\omega) = \sigma'(\omega) + j\sigma''(\omega)$ can be determined from the complex permittivity using the following relationships.

$$\nabla \times H = J + \partial_t D \tag{2.7}$$

$$D = \epsilon^* \epsilon_0 E \tag{2.8}$$

$$J = \sigma^* E \tag{2.9}$$

$$\sigma^* = j\omega\epsilon^* \epsilon_0 \tag{2.10}$$

2.2.2.1 Kramers-Kronig relations

The Kramers-Kronig relations between the real and imaginary parts of the complex permittivity are of great importance. These relationships allow only one part of the permittivity to be used to fully represent the dielectric spectra; which is why I only show the imaginary part of the permittivity in this thesis. Additionally, because the Kramers-Kronig relations allow the complete dielectric response to be characterized by one part of the complex permittivity, it allows only one part of the permittivity to be measured. Measuring one part of the complex permittivity may be advantageous because it could allow for greater measurement sensitivity or accuracy. Jonscher develops the Kramers-Kronig relationships from the time-dependent dielectric response (17). Jonscher first defines the time dependent displacement noting that all physical systems will have a delayed material response to an external applied field. In the time dependent equation for displacement the material response is captured in the time dependent polarization $P(t)$.

$$D(t) = \epsilon_0 E + P(t) \tag{2.11}$$

Jonscher next defines the response function $f(t)$ as the material polarization in response to a delta function excitation $E\Delta t$, such that in the limit as $\Delta t \to 0$ the product $E\Delta t$ remains constant.

$$P(t) = \epsilon_0 (E\Delta t) f(t) \tag{2.12}$$

Using the response function we can build the material response for any excitation because the time-dependent excitation can be represented as an impulse chain of delta function excitations and

importantly, because the material system is causal, linear and time invariant. The second condition means that the material response can be represented as the sum of time shifted and amplitude scaled impulse responses. These conditions result in a convolution integral for the material polarization.

$$P(t) = \epsilon_0 \int_0^\infty f(t)E(t-\tau)d\tau \tag{2.13}$$

The Fourier transform of this convolution integral into the frequency domain results in a multiplication.

$$P(\omega) = \epsilon_0 \chi^*(\omega)E(\omega) \tag{2.14}$$

where $\chi^*(\omega)$, the electrical susceptibility related to the permittivity via $\epsilon^*(\omega) = \chi^*(\omega) + 1$, is now the Fourier transform of the response function $f(t)$

$$\chi(\omega) = \chi'(\omega) - j\chi''(\omega) = \int_0^\infty f(t)\exp(-j\omega t)dt \tag{2.15}$$

$$\chi'(\omega) = \int_0^\infty f(t)\cos(\omega t)dt \tag{2.16}$$

$$\chi''(\omega) = \int_0^\infty f(t)\sin(\omega t)dt \tag{2.17}$$

Looking at the resulting functions for the components of the susceptibility, Jonscher points out that because the two components of the susceptibility are dependent upon the same response function $f(t)$ it should possible to eliminate the response function and show that the two components are related to each other (17). By incorporating the following relationship from complex analysis the Kramers-Kronig relations are found, where $\not\int$ represents the Cauchy principal value (17).

$$\frac{1}{\pi}\not\int_{-\infty}^{\infty} \frac{\sin(xt)}{x-\omega}dx = \cos(\omega t) \tag{2.18}$$

$$\chi'(\omega) = \frac{1}{\pi}\not\int_{-\infty}^{\infty} \frac{\chi''(x)}{x-\omega}dx \tag{2.19}$$

$$\chi''(\omega) = -\frac{1}{\pi}\not\int_{-\infty}^{\infty} \frac{\chi'(x)}{x-\omega}dx \tag{2.20}$$

In summary, because the material response is from a physically real system it must be causal (i.e. the field induced change in polarization cannot precede the application of the field). As a consequence of causality the real and imaginary parts of the Fourier transform of the response

function are related by the Kramers-Kronig relations. This relationship means that only one of the components of the permittivity or susceptibility is necessary to fully describe the dielectric spectra. However, the Kramers-Kronig relationships do not capture the affect of DC conductivity which is only reflected in the measured imaginary part of the permittivity. The Kramers-Kronig relations apply to the time dependent material response and do not include the DC conduction because it is independent of time or frequency. This can be seen by examining the constitutive equation for the time dependent current density, where the material response $f(t)$ incorporates an instantaneous DC value and a time dependent component. The causal time dependence of the response function inevitably leads to similar Kramers-Kronig expressions as those shown for the electric susceptibility. Following the Fourier transformation of Equation 2.23 (where I have used the property that convolution in time is multiplication in frequency) and using Euler's identity for the complex exponential in the Fourier transform of the time dependent conductivity, it can be seen that the DC conductivity term σ_0 will add to the real part of the material response. Where there is a DC conductivity or a high frequency permittivity, the Kramers-Kronig relations cannot be directly applied to the measurement data. The data must first be corrected for the DC conductivity or high frequency permittivity in order to make the measured conductivity or permittivity Kramers-Kronig consistent. The time dependent AC conductivity will be captured in the dielectric response of the material, and can be retrieved using the relationships discussed in Section 2.2.2.

$$J(t) = \int_0^\infty f(\tau)E(t-\tau)d\tau \tag{2.21}$$

$$f(t) = \sigma_0\delta(t) + \tilde{\sigma}(t) \tag{2.22}$$

$$J(t) = \sigma_0 E(t) + \int_0^\infty \tilde{\sigma}(\tau)E(t-\tau)d\tau \tag{2.23}$$

$$J(\omega) = \sigma_0 E(\omega) + \left(\int_0^\infty \tilde{\sigma}(t)\exp\left(-j\omega t\right)dt\right)E(\omega) \tag{2.24}$$

$$J(\omega) = \sigma_0 E(\omega) + \left(\int_0^\infty \left[\tilde{\sigma}(t)\cos\left(\omega t\right) - j\tilde{\sigma}(t)\sin\left(\omega t\right)\right]dt\right)E(\omega) \tag{2.25}$$

The composites studied were found to be weak conductors which exhibit a small DC conductivity and AC conductivity. Because the conductivity of the samples is of interest to parameterize the

differences between the composites, I have chosen to plot the imaginary part of the permittivity for analysis.

2.2.3 Fitting procedure

The electrical properties of the metal powder composite samples were parameterized by fitting relaxation models to the processed data. Two behavior models were found to produce good fits for the samples. I will discuss the fitting procedure used for the two models in the following sections.

2.2.3.1 AC conductivity

The unoxidized powders M316L1 through M316L5 were fit using the AC conductivity model Equation 2.26 presented by Jonscher for hopping charge carrier systems with no dielectric loss peaks (17).

$$\sigma'(\omega) = \sigma_0 + A\omega^n \tag{2.26}$$

Because of the small parameter values, the model was modified to minimize numeric underflow when using the *nlinfit* function of MATLAB. Numeric underflow was identified by MATLAB via the ill defined Jacobian at the solution. The modified model is shown in Equation 2.27 where the DC conductivity term σ_0 has been replaced by 10^C and the coefficient for the AC conduction A has been replaced by 10^B. These modifications allow for MATLAB to search for larger parameter values during the fitting process.

$$\sigma'(\omega) = 10^C + 10^B\omega^n \tag{2.27}$$

Initial parameter estimates were gathered from plots of the AC conductivity. With reference to Figure 2.8, the log of the real conductivity becomes linear in the log of frequency at frequencies greater than 10^5 Hz. Two representative points in the linear region were selected and the equation for a line between the points was determined. Parameter estimates for the AC conductivity coefficient A and the exponent n were determined from the intercept and slope of the line. Parameter estimates for the DC conductivity σ_0 were gathered from the low frequency limit of the plot. A

weighted non linear fit was conducted using the *nlinfit* function of MATLAB. A weighted fit was used to incorporate the observation weights of the data so that the uncertainty in the fit parameters reflects the uncertainty in the data. The weighted fit utilized the inverse of the standard deviation of the mean for the observation weight. In this case, data which has more variability is punished during the fit by a lower observation weight. The results of the fit can be seen in Figure 2.9 where the two distinct power law relationships can be seen.

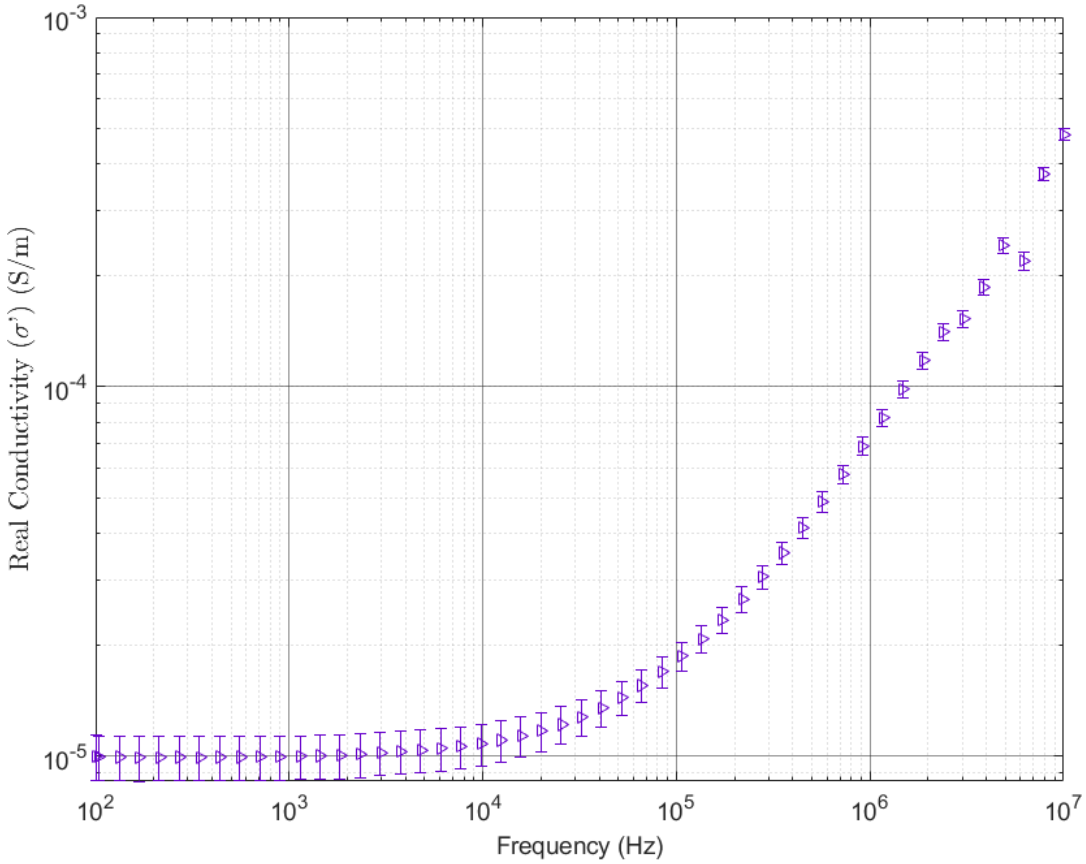

Figure 2.8 Plot of real conductivity $\sigma'(\omega)$ for powder M316L1. Each data value is the mean of 100 measurements. The reported uncertainty is the standard uncertainty multiplied by a coverage factor $k = 2$, providing a level of confidence of approximately 95%

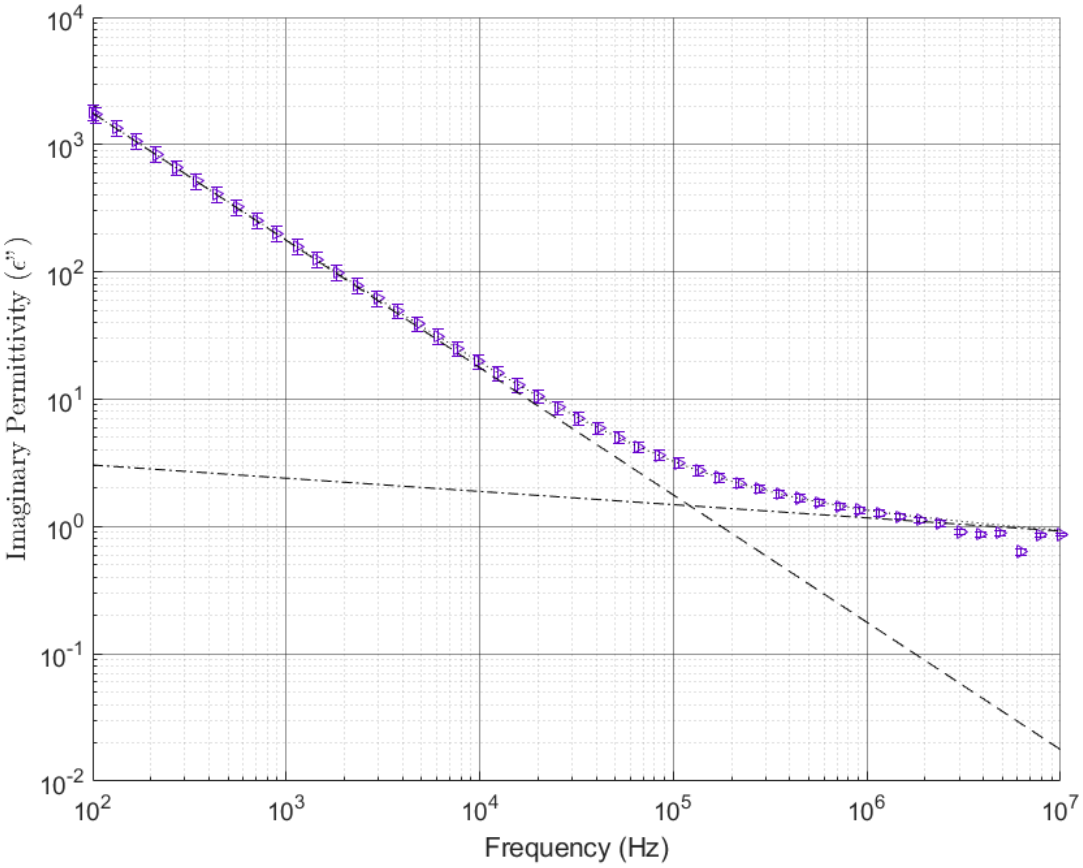

Figure 2.9 Plot of imaginary permittivity $\epsilon''(\omega)$ for powder M316L1. Each data value is the mean of 100 measurements. The reported uncertainty is the standard uncertainty multiplied by a coverage factor $k = 2$, providing a level of confidence of approximately 95%. The dashed line represents the DC conductivity contribution. The dash dot line represents the AC conductivity contribution.

2.2.3.2 Havriliak-Negami

The dielectric spectra of oxidized powders NNL1 and NNL2 were fit using a double Havriliak-Negami function shown in Equation 2.28.

$$\epsilon^*(\omega) = -j\left(\frac{\sigma_0}{\epsilon_0\omega}\right)^n + \sum_{k=1}^{2}\left[\frac{\Delta\epsilon_k}{(1+(j\omega\tau_k)^{\alpha_k})^{\beta_k}} + \epsilon_{\infty k}\right] \tag{2.28}$$

The fit was carried out using the winFIT software from Novocontrol Technologies. Initially, these powders were fit using the AC conductivity model from the previous section. Residuals from the AC conductivity model revealed the presence of a distinct relaxation peak in the dielectric spectra. To better model the relaxation peak the Havriliak-Negami function was selected. Initial parameter estimates were found by manually tuning the relaxation function after estimating the relaxation peak frequency. The results of this fitting process are shown in Figure 2.10

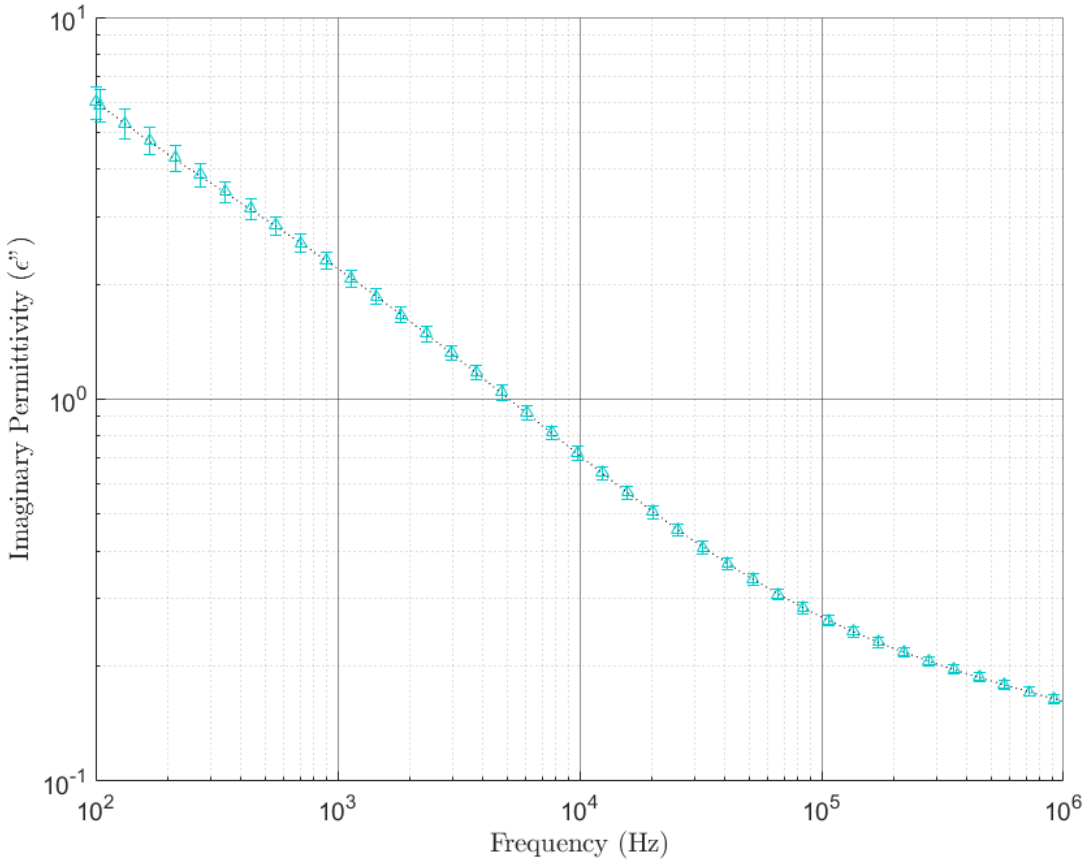

Figure 2.10 Plot of imaginary permittivity $\epsilon''(\omega)$ for powder NNL1. Each data value is the mean of 100 measurements. The reported uncertainty is the standard uncertainty multiplied by a coverage factor $k = 2$, providing a level of confidence of approximately 95%. The dotted line is the result of the fit in Equation 2.28.

CHAPTER 3. RESULTS

The following sections gather the results of the broadband dielectric spectroscopy measurements. The measured imaginary permittivity and real conductivity are plotted to show the differences between the metal powder wax composites. The fitting parameters have been tabulated with uncertainties provided by the *nlinfit* MATLAB function for powders M316L1 through M316L5 and the winFIT Novocontrol software for the oxidized powders NNL1 and NNL2. The reported uncertainty for the fitting parameters is at the 95% confidence level. For the figures shown, each data value is the mean of 100 measurements. The reported uncertainty in the figures is the standard uncertainty multiplied by a coverage factor $k = 2$, providing a level of confidence of approximately 95%. The standard uncertainty was determined in accordance with the International Organization for Standardization Guide to the Expression of Uncertainty in Measurement (25). It was found that the main source of experimental uncertainty was sample-to-sample variation in the ten replicate samples prepared for each powder. The sample-to-sample variation is captured in the standard error of the mean; which is used as the standard uncertainty. Because the sample-to-sample variation dominates the experimental uncertainty, other sources of experimental uncertainty such as geometric tolerances and instrument error are not considered.

3.1 Real conductivity

The real conductivity was extracted from the edge corrected capacitance values as described in Section 2.2 and shown in Figure 3.1. The unoxidized powders M316L1 through M316L5, which exhibit charge hopping DC conduction with no visible loss peaks, were fitted using the Jonscher model for AC conductivity described in 2.2.3.1

$$\sigma'(\omega) = 10^B + 10^C \omega^n$$

The tabulated values of the fitting parameters (B, C, n) and associated estimates of uncertainty are given in Table 3.1.

Table 3.1 AC conductivity fitting parameters for unoxidized powders M316L1 through M316L5. The reported uncertainty is the 95% confidence interval estimates calculated by MATLAB using the *nlparci* function.

	C, $\log A$	n	B, $\log \sigma_0$
M316L1	-10.28 ± 0.03	0.896 ± 0.005	-5.007 ± 0.001
M316L2	-7.2 ± 0.8	0.6 ± 0.1	-2.689 ± 0.003
M316L3	-9.11 ± 0.01	0.751 ± 0.002	-5.162 ± 0.002
M316L4	-10.74 ± 0.02	0.922 ± 0.003	-6.73 ± 0.01
M316L5	-10.61 ± 0.03	0.901 ± 0.004	-5.696 ± 0.003

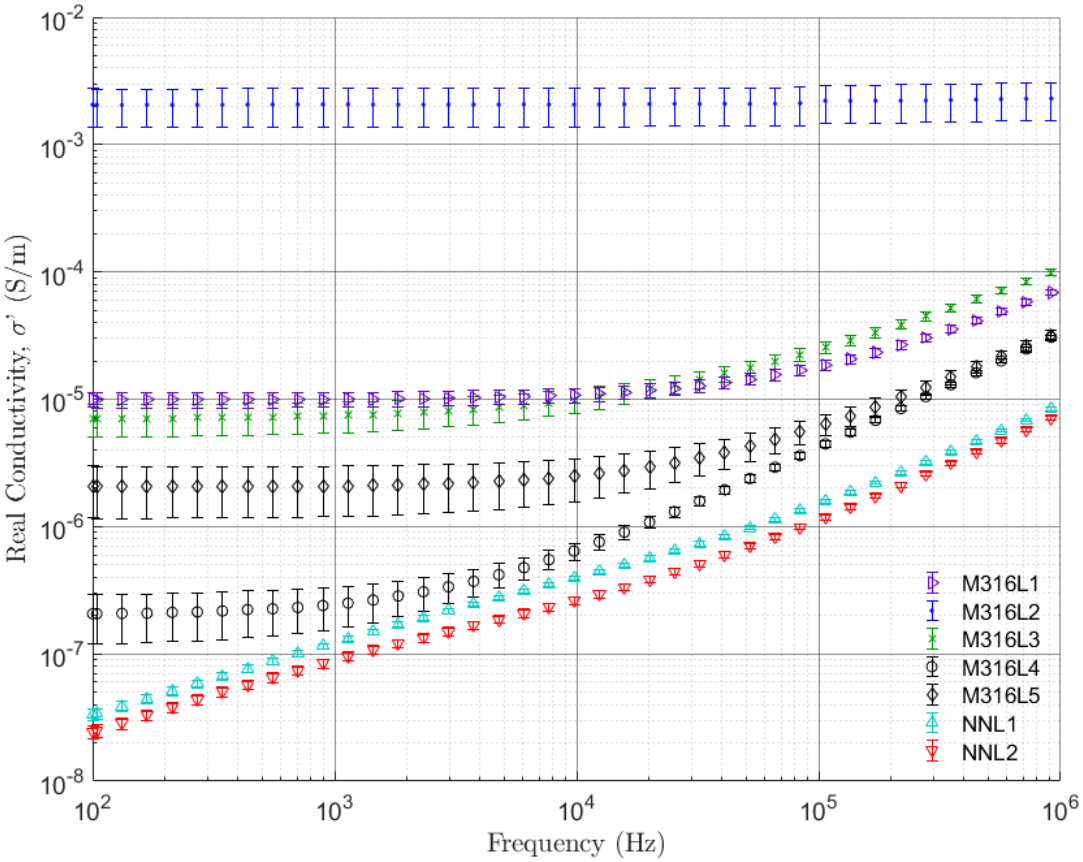

Figure 3.1 Comparison of metal powder composite real conductivity

3.2 Imaginary permittivity

The imaginary permittivity was extracted from the edge-corrected capacitance values as described in Section 2.2 and shown in Figure 3.2. The oxidized powders NNL1 and NNL2, which exhibit a visible loss peak, were fitted using the Havriliak-Negami model for dielectric relaxation described in 2.2.3.2. The tabulated values of the fitting parameters and associated estimates of uncertainty are in the following tables.

Table 3.2 DC conductivity parameters from the Havriliak-Negami fitting process

	σ_0 (S/cm)	n
NNL1	$(8.8 \pm 9.9) \times 10^{-10}$	$(6.0 \pm 1.7) \times 10^{-1}$
NNL2	$(4.1 \pm 6.9) \times 10^{-10}$	$(6.3 \pm 3.4) \times 10^{-1}$

Table 3.3 Havriliak-Negami function fitting parameters for oxidized powders NNL1 and NNL2, $k = 1$

	$\Delta\epsilon_1$	τ_1 (s)	$\epsilon_{1,\infty}$	α_1	β_1
NNL1	$(7.5 \pm 1.9) \times 10^{-1}$	$(0.2 \pm 1.4) \times 10^{-6}$	1.0000 Note	$(4.0 \pm 3.5) \times 10^{-1}$	1.0 ± 2.9
NNL2	$(7.0 \pm 0.9) \times 10^{-1}$	$(3.4 \pm 9.0) \times 10^{-7}$	1.0000 Note	$(4.1 \pm 1.7) \times 10^{-1}$	1.0 ± 1.3

Note: The uncertainty was to small to be reported by winFIT.

Table 3.4 Havriliak-Negami function fitting parameters for oxidized powders NNL1 and NNL2, $k = 2$

	$\Delta\epsilon_2$	τ_2 (s)	$\epsilon_{2,\infty}$	α_2	β_2
NNL1	3.4 ± 4.3	$(4.1 \pm 2.1) \times 10^{-4}$	1.0000 Note	$(6.6 \pm 2.2) \times 10^{-1}$	$(9.6 \pm 4.2) \times 10^{-1}$
NNL2	3.2 ± 5.1	$(7.4 \pm 6.0) \times 10^{-4}$	1.0000 Note	$(7.5 \pm 1.4) \times 10^{-1}$	$(8.4 \pm 1.8) \times 10^{-1}$

Note: The uncertainty was to small to be reported by winFIT.

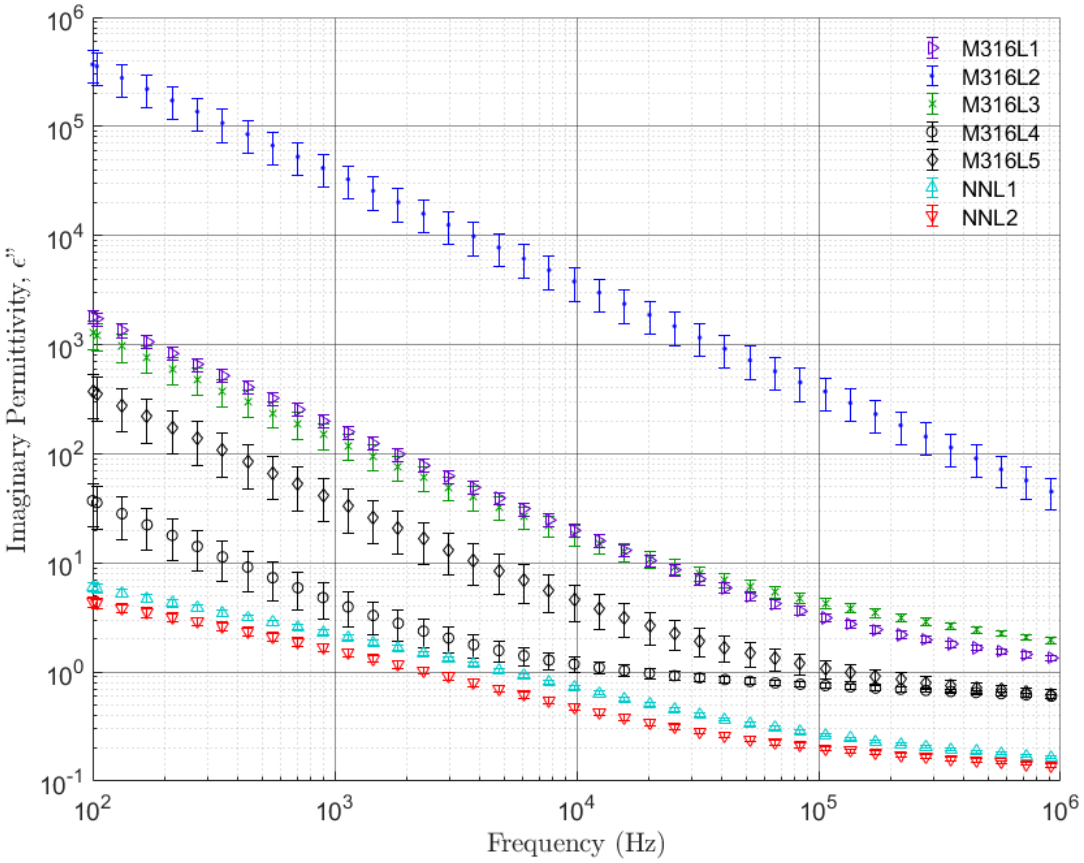

Figure 3.2 Comparison of metal powder composite imaginary permittivity

3.3 Observations and discussion

The broadband dielectric spectroscopy measurement results are broken down into three observation categories and discussed: size distribution, morphology, and surface oxidation. Within each category, the effects of the variation in the powder property on the dielectric spectra are discussed. In general it was observed that unoxidized powders M316L1 through M316L5 behaved as poor, charge hopping conductors with no observable loss peak in the frequency range examined and limited DC conductivity within the range of 10^{-7} to 10^{-3} S/m. Evidence for the charge hopping mechanism can be seen in the low frequency dispersion of the real part of the permittivity in Figure 3.3 and the low frequency dispersion of the real part of the conductivity in Figure 3.1. If the system were exhibiting solely DC conductivity, the low frequency behavior of the real permittivity would be independent of frequency as would the real conductivity (i.e the real permittivity and conductivity would be flat). The low frequency dispersion suggests that the DC conduction mechanism is also a polarization mechanism. As the composites studied are not ionic conductors this leads to the conclusion that the systems are exhibiting charge hopping conduction and polarization. The imaginary permittivity plot for powders M316L1 through M316L5 consists of two log-log linear regions. The two regions of behavior give evidence of two physically different relaxation mechanisms occurring in tandem. Additionally, the log-log linear behavior describes a relaxation mechanism whose losses are not dependent upon frequency but rather are constant per transition (16). The oxidized powders NNL1 and NNL2 showed the emergence of a loss peak within the frequency range examined and demonstrated more insulative behavior with very small DC conductivities on the order of 10^{-8} S/m. The emergence of the loss peak describes a polarization mechanism which has losses proportional to frequency or requires a constant time delay for a transition (16). Both dipolar processes, such as the reorientation of dipoles in a Debye model, and thermally activated single-particle transitions over potential barriers exhibit these behaviors. Determining the presence of a specific polarization mechanism in light of the available microscopic theory requires an analysis of the activation energy for the polarization mechanism. The activation energy can be estimated by measuring the dielectric response at different temperatures. With respect to the dielectric behavior

of the powder composites NNL1 and NNL2, it is expected that there will be dielectric responses of both a dipolar and charge hopping nature. The additional oxide layer may delay or alter the dipolar response of the metal particles; which form dipoles when exposed to a uniform electric field. The dipolar response of the metal particles is not visible in the dielectric response of powders M316L1 through M316L5 because the response is outside of the measured frequency range. The oxide may also present a barrier to thermally activated single-particle transitions by extending the distance between energetically favorable transition sites; thereby increasing the energy required for the transition or decreasing the transition rate (17).

3.3.1 Size distribution

Powders M316L1, M316L4, and M316L5 were modified by the manufacturer in order to allow the effects of changing the particle size distribution on the dielectric spectra to be examined. The particle size distributions can be seen in Figure 2.2, and are summarized as follows; M316L1 has a wide distribution, M316L4 has been depleted of fines (i.e. particles with dimension $\leq$ 25 μm have been removed), M316L5 has a bimodal distribution of larger particles $\sim$ 62 μm and smaller particles $\sim$ 25 μm. The real conductivity results show that composites which have a larger number of small particles (M316L1 and M316L5) have higher DC conductivity and transition frequency (ω_c) than powders which have been depleted of small particles (M316L4). This behavior may be explained by examining the possible percolation path lengths due to the metallic inclusions in the material. Figure 3.4 shows an example two dimensional material which initially is composed of ten large particles in a matrix. The area fraction of the inclusions in this material is

$$\text{area fraction} = \frac{\text{number of inclusions} \times \text{area of inclusion}}{\text{area total}} = \frac{10(\pi/4)D_1^2}{A_{total}} \tag{3.1}$$

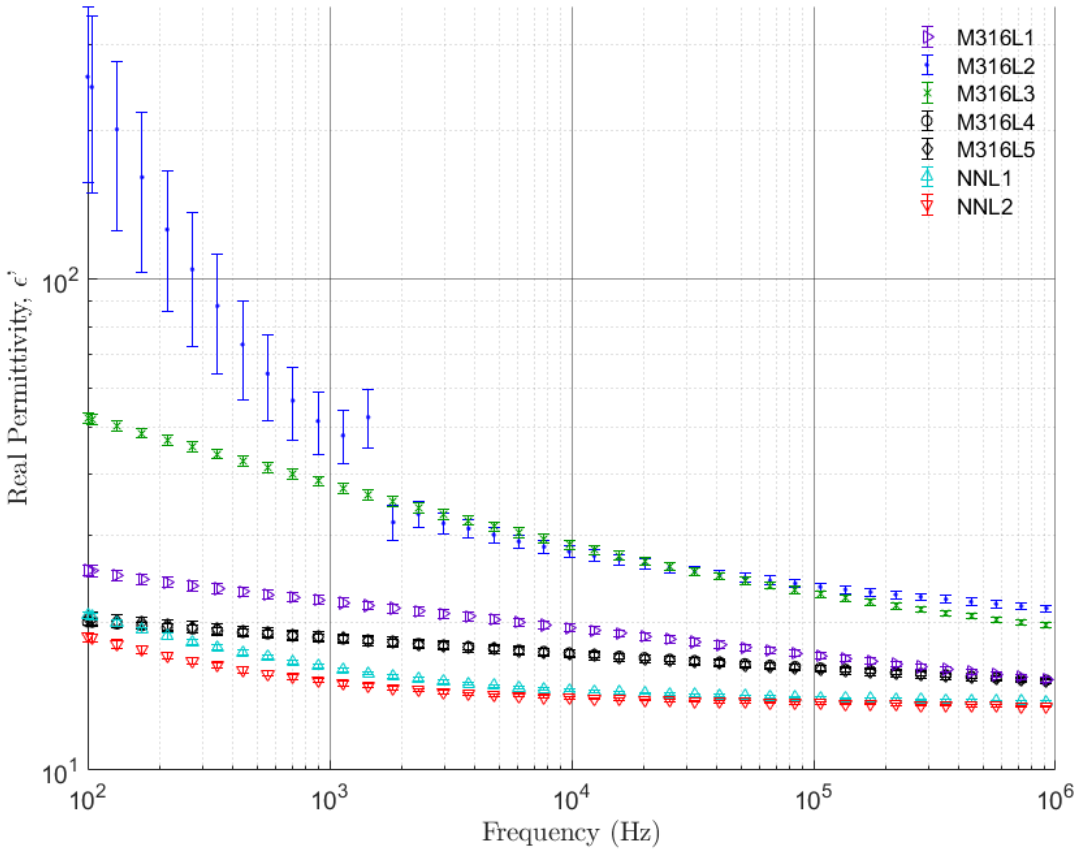

Figure 3.3 Plot of real permittivity $\epsilon'(\omega)$. Each data value is the mean of 100 measurements. The reported uncertainty is the standard uncertainty multiplied by a coverage factor $k = 2$, providing a level of confidence of approximately 95%.

Next, the material is modified to include small particles such that the area fraction remains the same and the powder is composed of 75% large particles and 25% small particles $C = (1/3)B$.

$$\frac{10(\pi/4)D_1^2}{A_{total}} = \frac{B(\pi/4)D_1^2}{A_{total}} + \frac{C(\pi/4)D_2^2}{A_{total}} \tag{3.2}$$

$$10D_1^2 = BD_1^2 + CD_2^2 \tag{3.3}$$

$$10D_1^2 = BD_1^2 + (1/3)BD_2^2 \tag{3.4}$$

$$B = \frac{10D_1^2}{D_1^2 + (1/3)D_2^2} \tag{3.5}$$

$$\tag{3.6}$$

Substituting for particle sizes representative of the powders $D_1 = 53$ μm and $D_2 = 25$ μm, gives the result $B = 9.3$ and $C = 3.1$. This result is shown in Figure 3.4. The effect of adding small particles while maintaining the same volume/area fraction is an increase in the possible linear span of the percolating networks. In this example losing one large particle results in the addition of approximately three small particles with an overall gain in possible linear span of approximately 22 μm. As the linear span of the percolating networks throughout the sample increases, the probability of forming a sample-wide conducting pathway increases, as well as the formation of multiple such parallel networks; causing an overall increase in conductivity.

3.3.2 Morphology

Powders M316L2 and M316L3 were modified by the manufacturer to change the particle morphology. Using water atomization in the manufacturing process creates highly irregular non-spherical shapes. M316L2 was designed to be the most irregularly shaped powder and is composed of prolate spheroids as seen in Figure 2.1. Powder M316L3 was designed to be more nearly spherical than M316L2. Two possible measures of the change in the particle morphology away from spherical are the apparent density and the powders flow ability. Spherical particles have higher packing fractions and therefore a higher apparent density. Irregularly shaped, non-spherical particles have higher ratios of surface area to volume. The increase in surface area causes greater interparticle friction which reduced the flow ability of the powder (28). A comparison of the manufacturer pro-

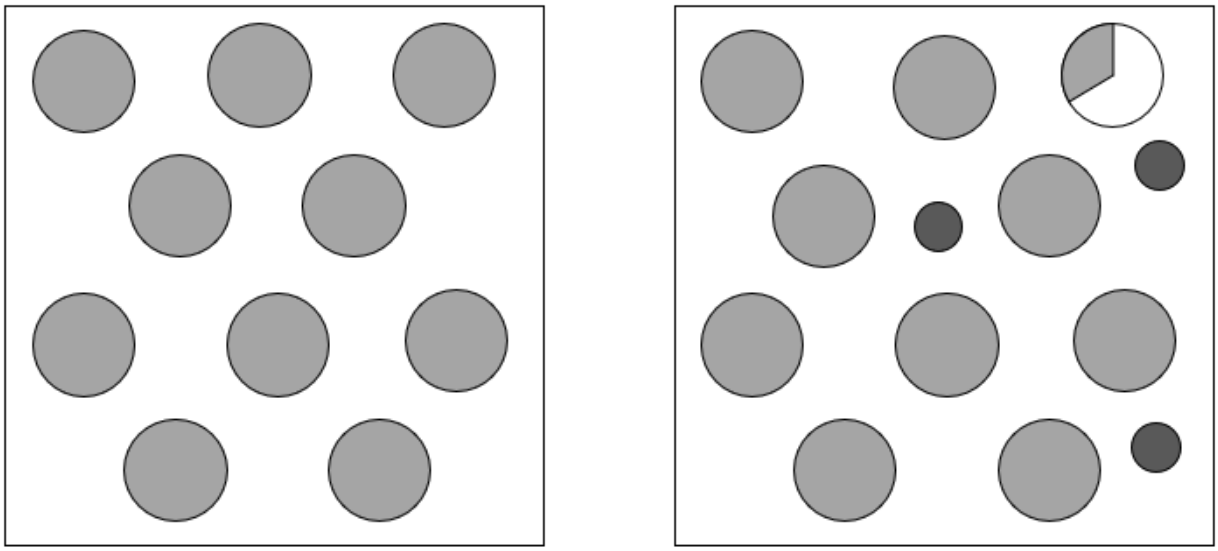

Figure 3.4 Example composite showing that for the same volume fraction, composites which contain smaller particles may have longer possible linear spans and greater probability of forming percolating pathways

vided flow ability and apparent density for powders M316L2 and M316L3 can be seen in Table 3.5. The M316L2 composite had the highest DC conductivity and sample to sample variability of the composites tested. The dielectric behavior of the M316L2 composite is nearly pure DC conduction as seen in Figure 3.2, where the log-log slope of the imaginary permittivity is nearly -1 and independent of frequency. However, the accompanying relaxation in the real permittivity shown in Figure 3.3 suggests that the DC conduction mechanism is also the polarization mechanism. This behavior follows the discussion in Section 1.3.3. Sillars demonstrated that elongation of the filler particles in the direction of the applied field results in an increase in the dielectric losses (22). Sillars also generalized his theory to randomly oriented ellipsoids finding that the assumption that the unique axis points along the direction of the applied field over estimates the permittivity by a factor of three (22). The experimental results confirm this theory and show that as the particles take on prolate spheroidal shapes as opposed to spherical shapes the dielectric losses increase.

Table 3.5 Comparison of the flow ability and apparent density for powders M316L2 and M316L3.

	Apparent Density (g/cc)	Flow (Sec/50g)
M316L2	2.82	28
M316L3	3.58	20

3.3.3 Surface oxidation

Powders NNL1 and NNL2 were prepared to examine the effect of increasing the surface oxidation of the 316L powder. NNL2 is nominally the more highly oxidized powder with a target oxygen content increase of 0.35% whereas NNL1 has a target oxygen content increase of 0.25%. The additional surface oxidation changes the nature of the dielectric response and adds a visible relaxation peak to the imaginary permittivity seen in Figure 3.2, this relaxation peak is not present for the unoxidized powders M316L1 through M316L5. The presence of the relaxation peak is explained by Jonscher as a polarization mechanism with frequency dependent loss or constant time required for transition (17). The additional surface oxide may be acting as a barrier to the charge hopping mechanism in the composites or altering the dipolar response of the metal particles. The observed shift in the relaxation frequency can be modeled with MWS relaxation at one of the interfacial boundaries (oxide to matrix and oxide to core metal) where there is a contrast in material properties. Because there are two interfaces it is expected that there will be another MWS relaxation peak. However, the second MWS relaxation peak was not observed, most likely because it occurs at a higher frequency outside of the frequencies measured in this study. The DC conductivity of the composite lowers as the oxygen content is increased. The NNL1 composite is nearly twice as conductive as the more oxidized NNL2 composite. Subtracting the DC conductivity contribution from the imaginary permittivity allows the relaxation peaks to be seen in greater detail as shown in Figure 3.5, where it can be seen that increasing the surface oxide thickness causes a shift in the relaxation peak frequency. The effect of the interfacial layer can be modeled using a modified Maxwell-Wagner-Sillars equation given in (15). As an example, the modified Maxwell-Wagner-Sillars equation is applied to a system designed to approximate the oxidized metal powder

composites. The system is composed of a dielectric matrix material with frequency independent conductivity and permittivity

$$\epsilon_m^* = \epsilon_m' - j\sigma_m/(\epsilon_0\omega)$$

an inclusion material with a 30% volume fraction made of a core of conductive material

$$\epsilon_f^* = \epsilon_f' - j\sigma_f/(\epsilon_0\omega)$$

and a shell of dielectric material with frequency independent conductivity and permittivity

$$\epsilon_l^* = \epsilon_l' - j\sigma_l/(\epsilon_0\omega)$$

The layer thickness was varied from near zero to a final layer thickness of 5% of the core radius. Additionally, the layer thickness increases at the expense of the matrix. The results of the model are shown in Figure 3.6. The Figure shows that as the layer thickness is increased the relaxation peak frequency shifts to lower frequencies and the dielectric losses increase; which is the behavior observed in Figure 3.5. The results of this approximation suggest that the cause of the relaxation peak observed in the imaginary permittivity may be interfacial polarization at the matrix to oxide or oxide to core interfaces. The surface oxide of powders NNL1 and NNL2 was further characterized by the Naval Nuclear Laboratory using Auger electron spectroscopy (AES). The surface of representative particles were bombarded with ions to remove material in a controlled fashion while monitoring the oxygen content of the particle by analyzing the AES spectra. The oxide layer thickness was estimated from the oxygen depth profile. An example of the depth profile can be seen in Figure 3.7. The results of the AES analysis give the oxide layer for NNL1 as $\approx$ 1000Å and NNL2 as $\approx$ 1000Å $-$ 2000Å. Therefore, broadband dielectric spectroscopy can distinguish the change in oxide layer thickness on the order of hundreds of nanometers.

Table 3.6 Parameter values used in the modified MWS equation to show the effect of the oxide layer.

	ϵ'	σ (S/m)
Matrix	2.7	1.26×10^{-6}
Core	1	1×10^{6}
Shell	14.2	4×10^{2}

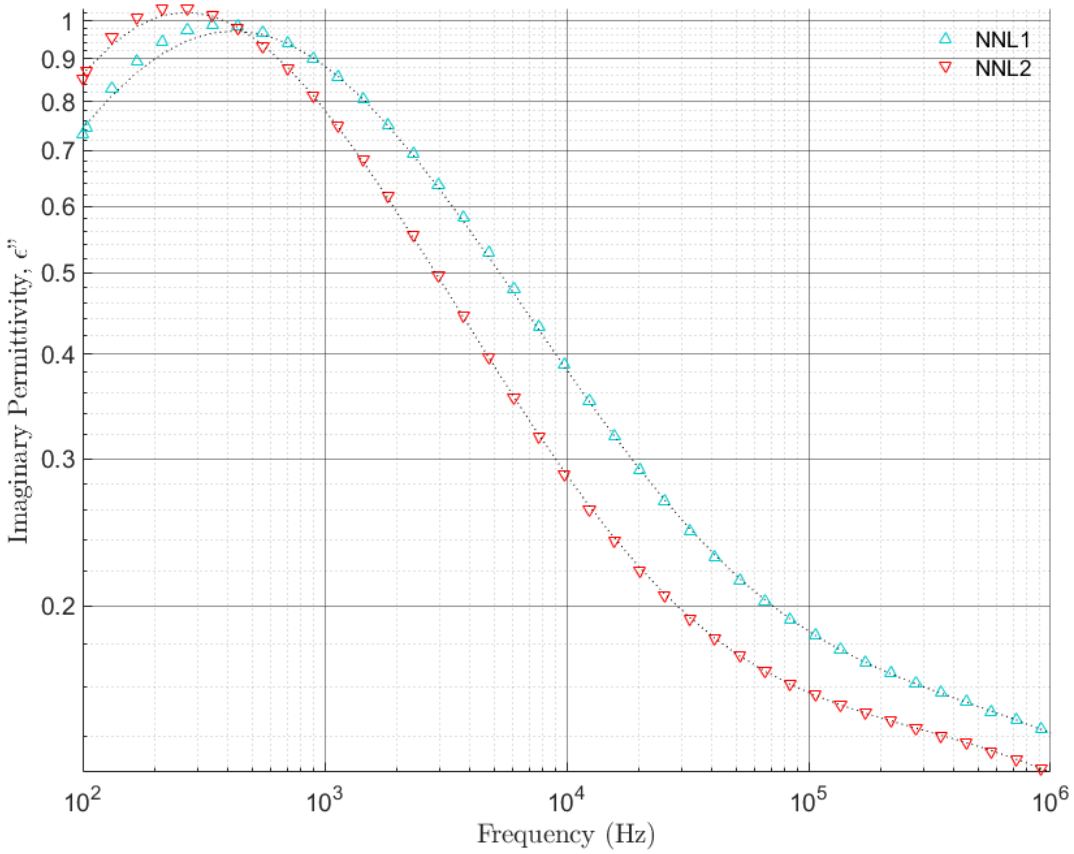

Figure 3.5 Plot of imaginary conductivity for NNL1 and NNL2 composites with DC conductivity contribution removed.

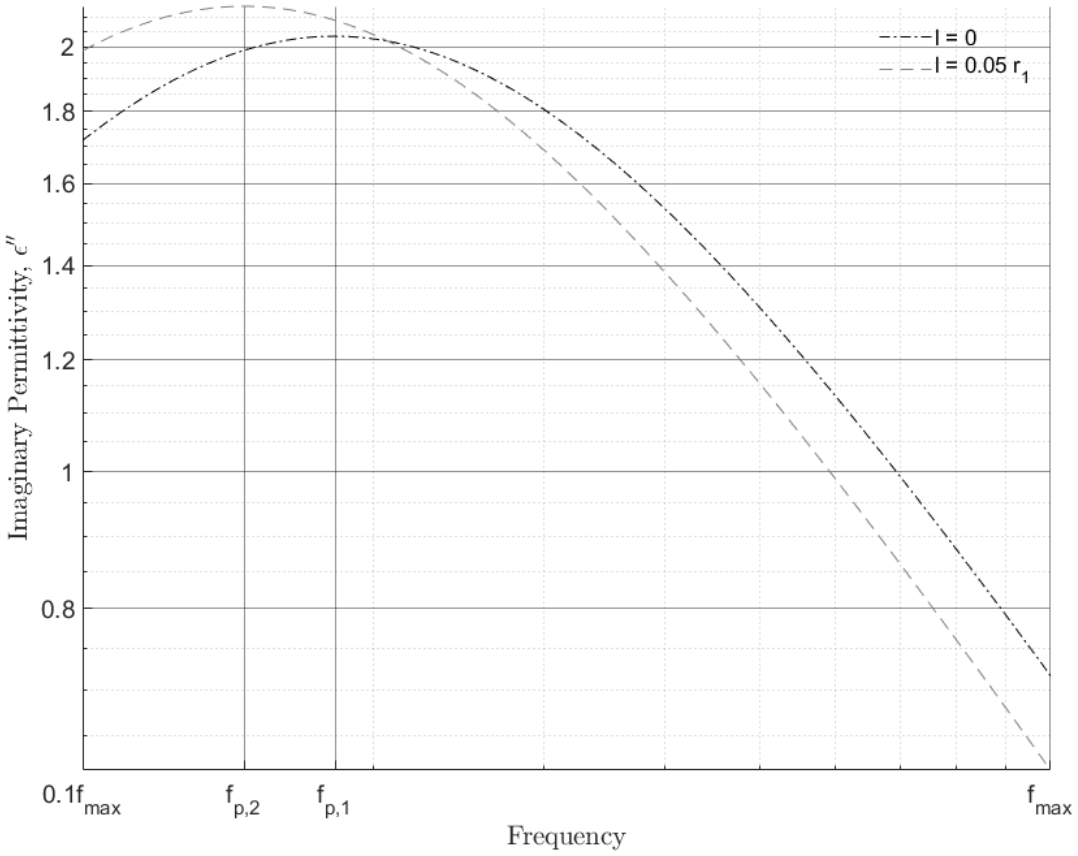

Figure 3.6 Results of modified MWS model with parameter values from Table 3.6 showing the shift in the relaxation peak frequency as the layer thickness is increased.

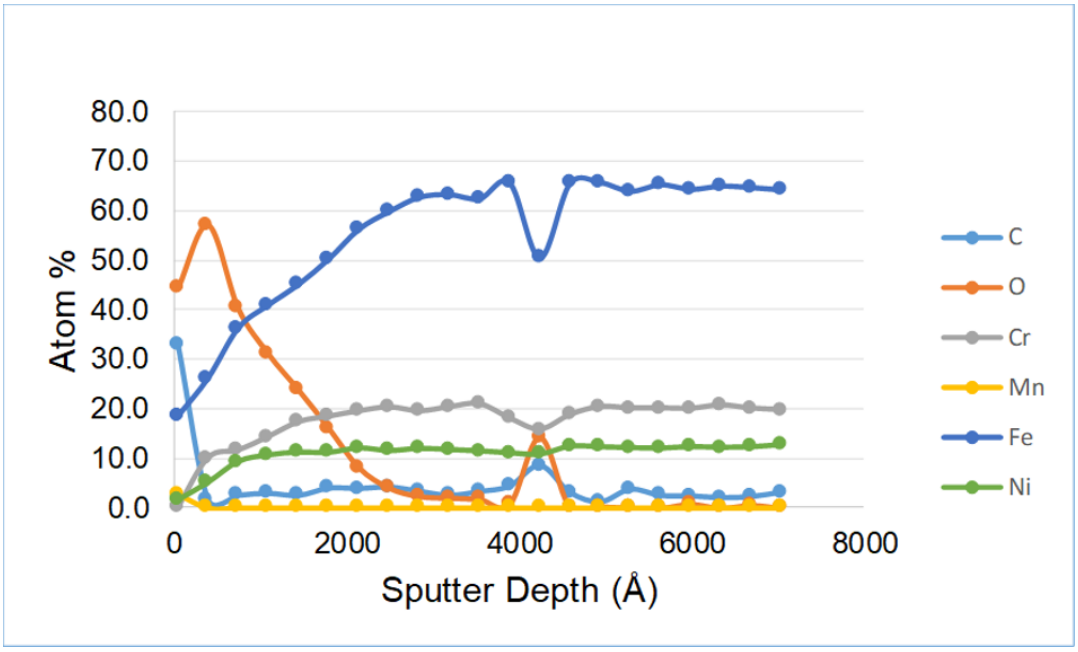

(a)

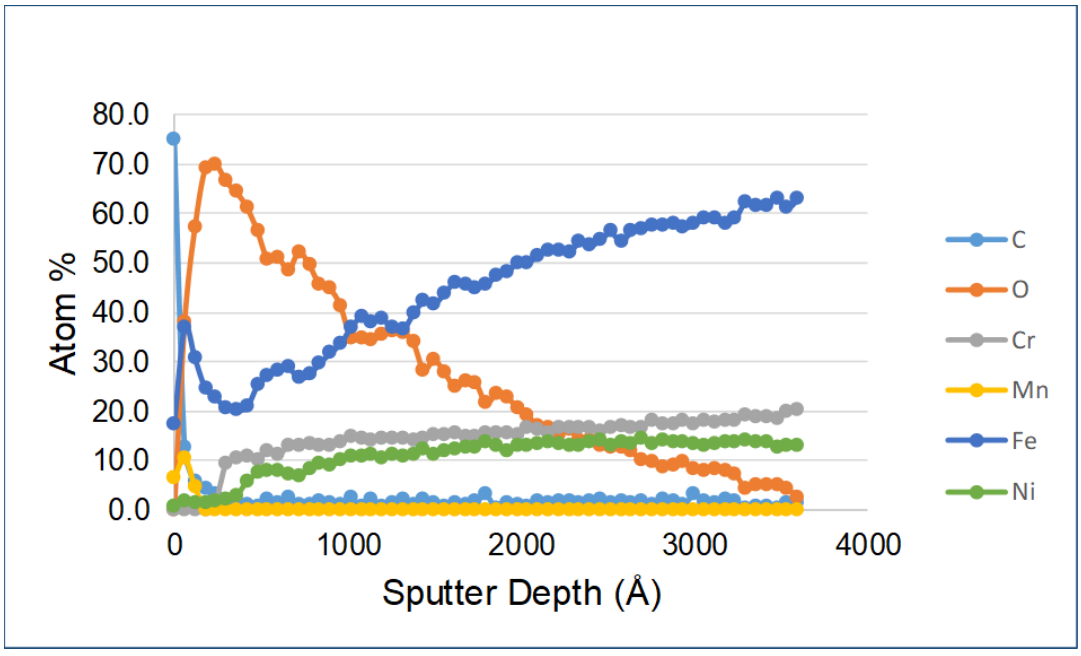

(b)

Figure 3.7 (a) AES depth profile for a representative particle from powder NNL1. (b) AES depth profile for a representative particle from powder NNL2. The depth profile shows the decrease in the oxygen content with depth, giving an estimate of the oxide layer thickness. Source: NNL courtesy of Michael Burrell.

3.4 Conclusion

In summary, the goal of this research is to assess the feasibility of using the electrical properties of the metal feed powder to characterize the overall quality of the feed powder used in additive manufacturing. Seven metal powders were fabricated or modified to model the possible changes which occur in the feed powder during the additive manufacturing process. The powders were modified to create differences in size distribution, particle morphology, and degree of surface oxidation. The electrical properties of the powder were measured by incorporating the powder into paraffin wax-based composites; which were then shaped into suitable samples for measurement. The electrical properties of the composites were then measured using broadband dielectric spectroscopy. It was found that the changes in size distribution, morphology, and surface oxidation were detectable using broadband dielectric spectroscopy. Removing small particles from the powder was shown to lower the DC conductivity of the metal powder wax composite. Changes to the particle morphology caused by the water atomization fabrication technique caused an increase in the DC conductivity of the composite. The development or growth of the surface oxide causes a significant change in the dielectric behavior of the composites with the emergence of a loss peak in the dielectric spectra. The position of the loss peak is related to the thickness of the oxide layer. These findings support the hypothesis that the changes in the feed powder through the additive manufacturing process will cause a change in the powders complex permittivity; which can then be detected using broadband dielectric spectroscopy. The results of this research show that it is feasible to use the electrical properties of the metal feed powder to characterize the powder, and can serve as the basis for the future development of online nondestructive evaluation methods to monitor the changes in the feed powder throughout the additive manufacturing process.

There are several nondestructive evaluation techniques to measure the permittivity of a substance such as; capacitive methods using interdigital capacitors, coaxial probe, resonant cavity, and transmission line methods. These various methods could be incorporated into the powder bed fusion system to scan the surface of the powder bed or incorporated into the powder delivery mechanism to measure the feed powder properties. Future work should examine the sensitivity of these various

techniques to the changes in the feed powder properties and monitor the change in feed powder properties throughout several build cycles. The use of advanced nondestructive evaluation sensors could enable the intelligent setting and modification of process parameters throughout the build process. Current additive manufacturing systems operate open loop; which means that there is no feedback from the system to aid in setting the process parameters. Without system feedback the technicians operating the system must adjust process parameters until the built part is satisfactory. Incorporating nondestructive sensors would help to close the loop by giving technicians valuable feedback and ensure consistent high quality part production while maximizing feed powder reuse.

BIBLIOGRAPHY

[1] D. D. Gu, W. Meiners, K. Wissenbach, and R. Poprawe, "Laser additive manufacturing of metallic components: materials, processes and mechanisms," *International Materials Reviews*, vol. 57, no. 3, pp. 133–164, 2012.

[2] "Formnext 2019 exhibitor list." https://formnext.mesago.com/frankfurt/en/exhibitor-search.html. Accessed: 2020-03-03.

[3] D. Gu, *Laser Additive Manufacturing of High-Performance Materials*. Springer, 1st ed., 2015.

[4] J.-P. Kruth, P. Mercelis, J. Van Vaerenbergh, L. Froyen, and M. Rombouts, "Binding mechanisms in selective laser sintering and selective laser melting," *Rapid Prototyping Journal*, vol. 11, no. 1, pp. 26–36, 2005.

[5] H. Taheri, M. R. B. M. Shoaib, L. W. Koester, T. A. Bigelow, P. C. Collins, and L. J. Bond, "Powder-based additive manufacturing - a review of types of defects, generation mechanisms, detection, property evaluation and metrology," *International Journal of Additive and Subtractive Materials Manufacturing*, vol. 1, no. 2, pp. 172–209, 2017.

[6] K. Antony and N. Arivazhagan, "Studies on energy penetration and Marangoni effect during laser melting process," *J Eng Sci Technol*, vol. 10, no. 4, pp. 509–525, 2015.

[7] C. Kamath, B. El-Dasher, G. F. Gallegos, W. E. King, and A. Sisto, "Density of additively-manufactured, 316L SS parts using laser powder-bed fusion at powers up to 400 W," *The International Journal of Advanced Manufacturing Technology*, vol. 74, no. 1-4, pp. 65–78, 2014.

[8] E. Liverani, S. Toschi, L. Ceschini, and A. Fortunato, "Effect of selective laser melting (SLM) process parameters on microstructure and mechanical properties of 316L austenitic stainless steel," *Journal of Materials Processing Technology*, vol. 249, pp. 255–263, 2017.

[9] C. Wang, X. Tan, E. Liu, and S. B. Tor, "Process parameter optimization and mechanical properties for additively manufactured stainless steel 316L parts by selective electron beam melting," *Materials & Design*, vol. 147, pp. 157–166, 2018.

[10] L. Grainger, "Investigating the effects of multiple re-use of Ti6Al4V powder in additive manufacturing (AM)," *Renishaw plc*, 2016.

[11] D. Galicki, F. List, S. Babu, A. Plotkowski, H. Meyer, R. Seals, and C. Hayes, "Localized changes of stainless steel powder characteristics during selective laser melting additive manufacturing," *Metallurgical and Materials Transactions A*, vol. 50, no. 3, pp. 1582–1605, 2019.

[12] M. J. Heiden, L. A. Deibler, J. M. Rodelas, J. R. Koepke, D. J. Tung, D. J. Saiz, and B. H. Jared, "Evolution of 316L stainless steel feedstock due to laser powder bed fusion process," *Additive Manufacturing*, vol. 25, pp. 84–103, 2019.

[13] F. Pinto, I. Souza Filho, M. Sandim, and H. Sandim, "Defects in parts manufactured by selective laser melting caused by δ-ferrite in reused 316L steel powder feedstock," *Additive Manufacturing*, vol. 31, p. 100979, 2020.

[14] B. Sartin, T. Pond, B. Griffith, W. Everhart, L. Elder, E. Wenski, C. Cook, D. Wieliczka, W. King, A. Rubenchik, *et al.*, "316L powder reuse for metal additive manufacturing," in *Proceedings of the 28th Annual International Solid Freeform Fabrication Symposium*, pp. 351–364, 2017.

[15] F. Kremer and A. Schönhals, *Broadband dielectric spectroscopy.* Berlin ; New York: Springer, 2003.

[16] A. K. Jonscher, "Dielectric relaxation in solids," *Journal of Physics D: Applied Physics*, vol. 32, no. 14, pp. R57–R70, 1999.

[17] A. K. Jonscher, *Dielectric relaxation in solids.* London: Chelsea Dielectrics Press, 1983.

[18] P. J. W. Debye, *The collected papers of Peter J. W. Debye.* New York: Interscience Publishers, 1954.

[19] Novocontrol Technologies, "Frequency Domain Measurement." https://www.novocontrol.de/php/intro_freq_domain.php, 2020. [Online; accessed 26-April-2020].

[20] J. C. Maxwell, *A treatise on electricity and magnetism.* Clarendon Press series, Oxford: Clarendon, 3rd ed., 1904.

[21] K. W. Wagner, "Erklärung der dielektrischen nachwirkungsvorgänge auf grund maxwellscher vorstellungen," *Archiv für Elektrotechnik*, vol. 2, no. 9, pp. 371–387, 1914.

[22] R. Sillars, "The properties of a dielectric containing semiconducting particles of various shapes," *Journal of the Institution of Electrical Engineers*, vol. 80, no. 484, pp. 378–394, 1937.

[23] J. C. Maxwell Garnett, "Colours in metal glasses and in metallic films," *Proceedings of the Royal Society of London*, vol. 73, no. 488-496, pp. 443–445, 1904.

[24] H. G. Brittain, "Particle-size distribution, Part III: determination by analytical sieving," *Pharmaceutical Technology*, vol. 26, no. 12, pp. 56–64, 2002.

[25] Joint Committee for Guides in Metrology, "JCGM 100: Evaluation of Measurement Data - Guide to the Expression of Uncertainty in Measurement," tech. rep., JCGM, 2008.

[26] D. R. Lide, ed., *CRC handbook of chemistry and physics*. CRC press, 85th ed., 2004.

[27] Novocontrol Technologies, "ZGS Alpha Active Sample Cell." https://www.novocontrol.de/php/sa_cell_bdc.php, 2020. [Online; accessed 26-April-2020].

[28] K. Ridgway and R. Rupp, "The effect of particle shape on powder properties," *Journal of Pharmacy and Pharmacology*, vol. 21, no. S1, pp. 30S–39S, 1969.